Numerical simulations of compressible mixing layers

Tilo Lumpp, Hervé Guillard

INRIA

INSTITUT NATIONAL DE RECHERCHE EN INFORMATIQUE ET EN AUTOMATIQUE

Numerical Simulations of Compressible Mixing Layers

Tilo LUMPP
Hervé GUILLARD

N° 2217
Mars 1994

PROGRAMME 6

Calcul scientifique,
modélisation et
logiciels numériques

Numerical Simulations of Compressible Mixing Layers

Tilo Lumpp and Hervé Guillard

INRIA Sophia-Antipolis
2004, Route des Lucioles, B. P. 93
F-06902 Sophia-Antipolis Cedex

Numerical Simulations of Compressible Mixing Layers

T. Lumpp and H. Guillard

Abstract

The capability of second-order MUSCL-schemes to simulate compressible transitional flow is numerically investigated. The chosen test case concerns a temporally growing mixing layer for convective Mach-numbers between 0.3 and 0.8. Apart from an important reduction of the amplification rates of the perturbations, this type of flow shows the appearence of eddy shocklets that make necessary the use of numerical methods capable to capture structures which size is less than the grid size. It is shown that for high convective Mach numbers the necessary number of grid points is considerably larger than for incompressible or subsonic computations and in addition that unresolved MUSCL- methods may exhibit non-physical behaviors. This restricts the use of second-order MUSCL-schemes to low convective Mach numbers.

Simulation numérique de couches de mélanges compressibles

T. Lumpp et H. Guillard

Résumé

Ce travail étudie la capacité des méthodes de volumes finis du second-ordre de type "MUSCL" à simuler des écoulements transitionnel en régime compressible. Le cas test choisi est constitué d'une couche de mélange temporelle pour des nombres de Mach convectifs situés entre 0.3 et 0.8. En plus d'une réduction notable des taux d'amplifications des perturbations, ce type d'écoulements se caractérise par l'apparition de petits chocs qui rendent nécessaire l'utilisation de méthodes numériques capable de "capturer" des discontinuités de taille inférieure à la maille de calcul. On montre ici que les méthodes de type MUSCL nécessitent un grand nombre de points de discrétisation lorsque le nombre de Mach convectif croît et de plus que ces méthodes peuvent avoir des comportements non physiques. En définitive l'utilisation de telles méthodes doit être confiné à des Mach convectif assez faibles.

Contents

1 Introduction

The modelization of compressible turbulence is still in its infancy and detailed studies of simple flows are necessary to investigate and calibrate the models. A good example of such simple flow where the effect of compressibility can be isolated independently of any boundary influences is the mixing layer where two parallel flows mix under the effect of Kelvin-Helmholtz type instabilities. Linear Stability analysis reveals that at high convective Mach numbers, this flow presents interesting features with respect to its incompressible counterpart.
Michalke [5] made an often-cited linear stability analysis of a hyperbolic-tangent velocity-profile, supposing an incompressible and inviscid fluid. In extending this result to compressible flow, Blumen [2] discovered a large influence of the convective Mach-number on the amplification factor of subsonic instabilities. In a second study Blumen et al. [3] found a second mode of instability for supersonic convective mach-numbers being interpreted as supersonic instability modes. In a recent study, Sandham and Reynolds [11] exploited the results of [2]. The results of their numerical studies confirm most of the results predicted by linear stability analysis.

Direct Numerical Simulation (DNS) of compressible free shear layers have been appearing in the last few years using either Euler or Navier-Stokes equations. Several numerical methologies have been used : For shock-free flow, high-resolving spectral methods are the methods of choice : They have been used successfully for simulation of shear-flow, as was shown e. g. by Guillard et. al [4], who made simulations with convective Mach-numbers of up to 0.8. Tsilanizara [12] developped a spectral method for high-Reynolds-number flow and applied it to shear-flow with supersonic convective Mach-Numbers of up to 1.5. But spectral methods suffer from two important restrictions: They are very expensive in term of CPU-cost and they fail if shocks appear.
To overcome these difficulties, several recent studies have used high-order methods for simulating shear-flow with shocks. Lele [6] uses a fourth-order Padé-method to simulate shear-flow, while Shu et al. [10] show results obtained with third-order ENO-schemes. Nevertheless, the larger part of numerical investigations of compressible mixing layer has been done with simple second-order TVD-schemes which are cheap in terms of CPU cost and can handle shocks in a robust manner. However, these studies have also shown

that the stabilizing effect of the TVD-viscosity may have a strong influence on the accuracy of the solution:
Sandham and Yee [14] compare the solutions they obtained with several second-order TVD-schemes and come to the conclusion, that the limiting-process inherent in TVD-schemes introduces a considerable amount of numerical viscosity. This was also observed by Lu and Wu [7]. They compare their TVD-solutions to those obtained with an second-order ENO-scheme and remark also strong influence of the TVD-viscosity. Atkins [1] also observes spurious production of the first subharmonic in mixing layer simulation with second-order TVD-schemes.

This paper inquires into the necessity of high-order schemes for the simulation of shear-flow with shocks. Specifically, we investigate the performance of second-order MUSCL type schemes in term of accuracy with respect to the number of grid points, convective Mach-number and number of structures that are present in the computational box. It is organized as follows : After a short description of the numerical method and of the tools we found necessary to analyse flow with shocks, we compare the results obtained with a second-order FV-scheme with those of a spectral method. Then the investigation is extended to flow with shocks. In particular we investigate the influence of the grid-resolution on the solutions and look for grid-free results. In the last paragraph, we also comment briefly the effect of the physical viscosity on the growth of the mixing layer. The experiences are summarized and commented in the last section.

2 Governing equations and physical problem

The physical problem is a two-dimensional temporally developping mixing layer. The domain of calculation Ω is a rectangle of length L_x in horizontal direction and $2L_y$ in vertical direction, i. e.

$$0 \leq x \leq L_x \qquad\qquad -L_y \leq y \leq L_y \tag{1}$$

The Navier-Stokes-equations write in dimensionless form:

$$\frac{\partial \vec{q}}{\partial t} + \frac{\partial \vec{F}}{\partial x} + \frac{\partial \vec{G}}{\partial y} = \frac{1}{Re}\frac{\partial \vec{R}}{\partial x} + \frac{1}{Re}\frac{\partial \vec{S}}{\partial y} \tag{2}$$

The primitive variables of the fluid are density ρ, vector of velocities $\vec{u} = [u, v]^T$, pressure p, and temperature T. The vector of conservative variables is

$$\vec{q} = \begin{bmatrix} \rho \\ \rho u \\ \rho v \\ e \end{bmatrix} \qquad \text{with } e = \frac{p}{\gamma - 1} + \frac{1}{2}\rho(u^2 + v^2) \tag{3}$$

So e is the total energy of the fluid, $\gamma = \frac{c_p}{c_v} = 1.4$ is the ratio of the specific heats. The Euler fluxes in horizontal direction x and vertical direction y are

$$\vec{F} = \begin{bmatrix} \rho u \\ \rho u^2 + p \\ \rho uv \\ u(e+p) \end{bmatrix} \qquad \vec{G} = \begin{bmatrix} \rho v \\ \rho uv \\ \rho v^2 + p \\ v(e+p) \end{bmatrix} \tag{4}$$

The viscous fluxes are

$$\vec{R} = \begin{bmatrix} 0 \\ \tau_{xx} \\ \tau_{xy} \\ u\tau_{xx} + v\tau_{xy} + \frac{1}{PrMa^2(\gamma-1)}\frac{\partial T}{\partial x} \end{bmatrix} \vec{S} = \begin{bmatrix} 0 \\ \tau_{xy} \\ \tau_{yy} \\ u\tau_{xy} + v\tau_{yy} + \frac{1}{PrMa^2(\gamma-1)}\frac{\partial T}{\partial y} \end{bmatrix} \tag{5}$$

respectively.

The shear stresses are $\tau_{xx} = \frac{2}{3}\mu(2\frac{\partial u}{\partial x} - \frac{\partial v}{\partial y})$, $\tau_{xy} = \mu(\frac{\partial u}{\partial y} + \frac{\partial v}{\partial x})$, $\tau_{yy} = \frac{2}{3}\mu(2\frac{\partial v}{\partial y} - \frac{\partial u}{\partial x})$. In this study, the viscosity μ and the thermal conductiviy k are assumed to be a constant $(= 1)$.

In the above non-dimensionalized equations, the quantities ρ_∞, $2u_\infty$, T_∞, μ and k have been used, where the index ∞ denotes, that a quantity is taken at free-stream conditions. δ_i is the thickness of the shear layer at the beginning of the computation.

The dimensionless numbers (Reynolds number Re, Prandtl number Pr, Mach-number Ma) are defined by:

$$Re = \frac{2u_\infty \cdot \delta_i \cdot \rho_\infty}{\mu} \qquad Pr = \frac{c_p \mu}{k} \qquad Ma = \frac{2u_\infty}{\sqrt{\gamma R T_\infty}} \tag{6}$$

It is easily seen, that the reference Mach number defined here is twice the convective Mach number M_c. To complete the set of governing equations, it is necessary to give the equation of state in dimensionless form:

$$p = \frac{1}{\gamma Ma^2}\rho T \tag{7}$$

The basic flow is defined by a hyperbolic tangent velocity profile and is given by:

$$u_b = \frac{1}{2}\tanh(2y) \tag{8}$$

$$T = 1 + \frac{\gamma - 1}{2} \cdot \left(\frac{Ma}{2}\right)^2 \cdot (1 - (2u_b)^2) \tag{9}$$

$$\rho = \frac{1}{T} \tag{10}$$

$$p = \frac{1}{\gamma Ma^2} \tag{11}$$

A small perturbation is added to this basic flow. It is either a deterministic perturbation or a random one. The deterministic perturbation is defined by:

$$u = \frac{\epsilon y \lambda_{pert}}{20\pi} \cdot \sin(\frac{2\pi x}{\lambda_{pert}}) \cdot \exp(-\frac{1}{10}y^2) \tag{12}$$

$$v = \frac{\epsilon}{2} \cdot \cos(\frac{2\pi x}{\lambda_{pert}}) \cdot \exp(-\frac{1}{10}y^2) \tag{13}$$

It is easily verified that $\vec{\nabla} \cdot \vec{u} = 0$. λ_{pert} is the dimensionless wavelength of the perturbation. $\epsilon = 0.1$ is the amplitude of the deterministic perturbation.

The random perturbation is defined by :

$$u = \epsilon \cdot ran \cdot exp(-y^2) \tag{14}$$
$$v = \epsilon \cdot ran \cdot exp(-y^2) \tag{15}$$

ran is a random variable and $\epsilon = 0.005$ is the amplitude of the random perturbation.

The boundary conditions are the following:

- periodic in x:

$$\vec{q}|_{x=0} = \vec{q}|_{x=L_x} \qquad \left.\frac{\partial \vec{q}}{\partial x}\right|_{x=0} = \left.\frac{\partial \vec{q}}{\partial x}\right|_{x=L_x} \tag{16}$$

- slip conditions on the upper and lower boundary

$$\left.\frac{\partial \rho}{\partial y}\right|_{y=\pm L_y} = 0 \qquad \left.\frac{\partial p}{\partial y}\right|_{y=\pm L_y} = 0 \qquad \left.\frac{\partial u}{\partial y}\right|_{y=\pm L_y} = 0 \qquad v|_{y=\pm L_y} = 0 \tag{17}$$

In all computations a cartesian mesh was used. The grid is uniform in the x-direction and either uniform or stretched in the y-direction. So one gets for the mesh-sizes:

$$\Delta x = \frac{L_x}{N_x} = const. \tag{18}$$

while Δy is either

$$\Delta y = \frac{2 \cdot L_y}{N_y} = const. \tag{19}$$

or defined by a stretching parameter (see section 6.2) and N_x and N_y are the number of points in horizontal and vertical direction. The number of points varied from 101 to 401 points in x- and from 101 to 201 points in y-direction.

3 Solution method

We discuss briefly the finite-volume upwind scheme used in this study. Discretizing eq. 2 and manipulating gives:

$$\frac{\partial \vec{q}_{i,j}}{\partial t} = -\frac{1}{\Delta x \Delta y} \cdot \left(\Delta \vec{F}_{ij} \cdot \Delta y + \Delta \vec{G}_{ij} \cdot \Delta x - \frac{1}{Re} \Delta \vec{R}_{ij} \cdot \Delta y - \frac{1}{Re} \Delta \vec{S}_{ij} \cdot \Delta x \right) \tag{20}$$

where $\Delta \vec{F}_{i,j} = \vec{F}_{i+\frac{1}{2},j} - \vec{F}_{i-\frac{1}{2},j}$ is the difference of the flux $\vec{F}$ at the boundaries of the cell i,j. The flux-differences $\Delta \vec{G}, \Delta \vec{R}$ and $\Delta \vec{S}$ are similarly defined. A first order flux-function is defined by:

$$\vec{F}_{i+\frac{1}{2},j} = \frac{1}{2} \left(\vec{F}(\vec{q}^R) - \vec{F}(\vec{q}^L) \right) + \frac{1}{2} \left| \underline{\underline{A}} \right| \cdot \left(\vec{q}^R - \vec{q}^L \right) \tag{21}$$

where $\underline{\underline{A}}$ is the Roe matrice [9], and q^R and q^L are defined by $q^R = q_{i+1,j}$ and $q^L = q_{i,j}$ Analogous definitions are used for the flux G in y-direction.

This algorithm is of first order accuracy in space. To reach second order accuracy, a standard MUSCL-approach [13] is used. Here the primitive variables $\vec{w} = [\rho, u, v, p]^T$ are extrapolated from the left and the right side to the boundary of the computational cell. So we get for instance :

$$\vec{w}^R_{i+\frac{1}{2}} = \beta (\vec{w}_{i+2,j} - \vec{w}_{i+1,j}) - (1-\beta)(\vec{w}_{i+1,j} - \vec{w}_{i,j}) \tag{22}$$

$$\vec{w}^L_{i+\frac{1}{2}} = \beta (\vec{w}_{i+1,j} - \vec{w}_{i,j}) - (1-\beta)(\vec{w}_{i,j} - \vec{w}_{i-1,j}) \tag{23}$$

where β is an upwinding parameter:

- $\beta = \frac{1}{2} \Rightarrow$ Fromm' s scheme, second order
- $\beta = \frac{1}{3} \Rightarrow$ third order in the linear case

The conservative variables $\vec{q}^R$ and $\vec{q}^L$ are calculated with the extrapolated primitive variables:

$$\vec{q}^R = \vec{q}^R(\vec{w}^R) \tag{24}$$

$$\vec{q}^L = \vec{q}^L(\vec{w}^L) \tag{25}$$

and these values are used as arguments of the flux-function (21). In the computations presented here, no significant difference between the two values for β were observed. Noting eq. (20) under the form

$$\frac{\partial \vec{q}}{\partial t} = -\vec{Res} \tag{26}$$

we use a 5-step-Runge-Kutta-scheme for time-integration, that takes the form:

$$\begin{aligned}
\vec{q}^{(0)} &= \vec{q}^{n} \\
\vec{q}^{(1)} &= \vec{q}^{n} - \alpha_1 \vec{Res}(\vec{q}^{(0)}) \\
\vec{q}^{(2)} &= \vec{q}^{n} - \alpha_2 \vec{Res}(\vec{q}^{(1)}) \\
&\vdots \\
\vec{q}^{(5)} &= \vec{q}^{n} - \alpha_5 \vec{Res}(\vec{q}^{(4)}) \\
\vec{q}^{n+1} &= \vec{q}^{(5)}
\end{aligned}$$

with the coefficients $\alpha_1 = 0.059$, $\alpha_2 = 0.14$, $\alpha_3 = 0.273$ $\alpha_4 = 0.5$ and $\alpha_5 = 1.0$. This scheme is of second order accuracy, and the coefficients α_1 to α_5 were optimized to increase the stability properties of the scheme. The coefficients were published e. g. by Meinke and Hänel [8], and allow the use of CFL=4.0 in linear cases. But restrictions due to non-linearities appear, and in the examples that will be shown, the CFL-number was between 2.7 and 3.0.

4 Tools for analyzing the flow-field

4.1 Energy-spectra

The kinetic energy-spectra of the flow-field are obtained by:

$$e(k) = \frac{1}{2L_y} \int_{-L_y}^{L_y} |\hat{u}(k,y)|^2 + |\hat{v}(k,y)|^2 dy \tag{27}$$

where $\hat{u}(k,y)$ and $\hat{v}(k,y)$ are the Fourier-transforms of the horizontal and vertical components of the velocity-vector:

$$\hat{u}(k,y) = \frac{1}{L_x} \int_0^{L_x} u(x,y) \cdot exp(ikx) dx \tag{28}$$

$$\hat{v}(k,y) = \frac{1}{L_x} \int_0^{L_x} v(x,y) \cdot exp(ikx) dx \tag{29}$$

4.2 Helmholtz decomposition of the flow-field

The goal of this procedure is to find the part of the flow-field that contains the vortical structures and the part that contains the shocks, if they appear. It is based on the following result:
Any $\vec{u} \in L^2$ has the unique orthogonal decomposition

$$\vec{u} = \vec{u_i} + \vec{u_c} \tag{30}$$

such that $\vec{\nabla} \cdot \vec{u_i} = 0$ and there exists a scalar field Φ with $\vec{u_c} = \vec{\nabla}\Phi$. We have

$$||\vec{u_i}||_s \leq ||\vec{u}||_s \qquad \text{for any} \qquad s \geq 0. \tag{31}$$

We see that the velocity field $\vec{u}$ has been splitted in two orthogonal components $\vec{u_i}$ and $\vec{u_c}$ such that

$$\nabla \cdot \vec{u_c} = \nabla \cdot \vec{u} \qquad \text{and} \qquad \nabla \times \vec{u_c} = 0 \tag{32}$$

$$\nabla \cdot \vec{u_i} = 0 \qquad \text{and} \qquad \nabla \times \vec{u_i} \neq 0 \tag{33}$$

$$\int_{-L_y}^{L_y} \int_0^{L_x} \vec{u_c} \cdot \vec{u_i} d\vec{x} = 0 \tag{34}$$

Moreover, by (31) it is expected, that the "incompressible" part $\vec{u_i}$ is more regular than $\vec{u}$ is. The Helmholtz decomposition is performed by taking the divergence of eq. (30) to obtain:

$$\nabla \cdot \vec{u} = \nabla \cdot (\nabla\Phi) = \nabla^2\Phi \tag{35}$$

This elliptic equation is solved subject to homogeneous Neumann boundary conditions:

$$\frac{\partial \Phi}{\partial \vec{n}} = 0 \tag{36}$$

coming from the requirement that $\vec{u} \cdot \vec{n} = 0$. In this study (35 - 36) are solved by a simple second-order finite-difference scheme, while $\vec{\nabla} \cdot \vec{u}$ is also evaluated by a simple centered second order formula

5 Computations without shock

We first compare the results obtained with the presented method with those obtained with the spectral method of [4]. Two computations, one with a deterministic perturbation at a transonic convective Mach number and one with a random perturbation at a subsonic convective Mach number are shown.

5.1 Test 1: Subsonic case

The values of the parameters used for this test are:

$$Ma = 0.6 \quad (i.e. Ma_c = 0.3) \qquad Re = 1000 \qquad Pr = 0.7 \tag{37}$$

$$L_x = 15.06\delta_i \qquad L_y = 7.53\delta_i \tag{38}$$

The box length L_x corresponds to two times the wavelength the most amplified mode according to linear inviscid stability theory. The random perturbation is given by eqs. (14) and (15).

Figure 1 shows the contour lines of density ρ, Temperature T, Mach number Ma and entropy S obtained with the spectral algorithm, figure 2 shows the same quantities, for the second order FV-method at time $t = 95$. The differences between the numerical schemes are small, for both the shape and the extreme values. The difference of the extreme values does not exeed 8 % (table 1). The evolution of the vorticity thickness confirmes this result (fig. 3). The vorticity-thickness δ_ω is a often used measure for the growth of the

shear layer. It is defined by:

$$\delta_\omega = \frac{u_\infty - u_{-\infty}}{\left|\frac{\partial}{\partial y}\left(\frac{\overline{\rho u}}{\overline{\rho}}\right)\right|_{max}} \tag{39}$$

$\overline{\rho u}$ and $\overline{u}$ are the spatial averages in x-direction of ρu and ρ. The exact value of δ_ω at $t = 0$ is $\delta_\omega^0 = 1$. The only difference, one can observe between the two curves appears between the times $t = 55$ to $t = 75$ and reaches 12 %

Table 1: Extreme values of the contour-lines for FV-scheme (101 * 101 points) and spectral method (80 * 90 points), random perturbation

$T = 65$

Extreme value	FV-scheme	Spectral method	Difference (%)
ρ_{min}	0.9483	0.9281	2.18
ρ_{max}	1.0227	1.0330	1.0
S_{min}	1.9841	1.9841	0.0
S_{max}	2.0341	2.0347	0.03
T_{min}	0.9947	0.9911	0.36
T_{max}	1.0257	1.0261	0.04
Ma_{min}	$4.53 \cdot 10^{-3}$	$2.25 \cdot 10^{-3}$	—
Ma_{min}	0.3563	0.3869	7.9

$T = 95$

Extreme value	FV-scheme	Spectral method	Difference (%)
ρ_{min}	0.8546	0.8535	0.13
ρ_{max}	1.0432	1.0436	0.04
S_{min}	1.9836	1.9841	0.03
S_{max}	2.0385	2.0371	0.07
T_{min}	0.9562	0.9554	0.08
T_{max}	1.0196	1.0188	0.08
Ma_{min}	$2.925 \cdot 10^{-3}$	$8.98 \cdot 10^{-4}$	—
Ma_{min}	0.4793	0.4821	0.58

Figure 1: Contour lines of the spectral method, random perturbation, $90 * 80$ collocation points, $Ma_c = 0.3$, $Re = 1000$, $Pr = 0.7$, $L_x = 15.06 \cdot \delta_i$, $t = 95$

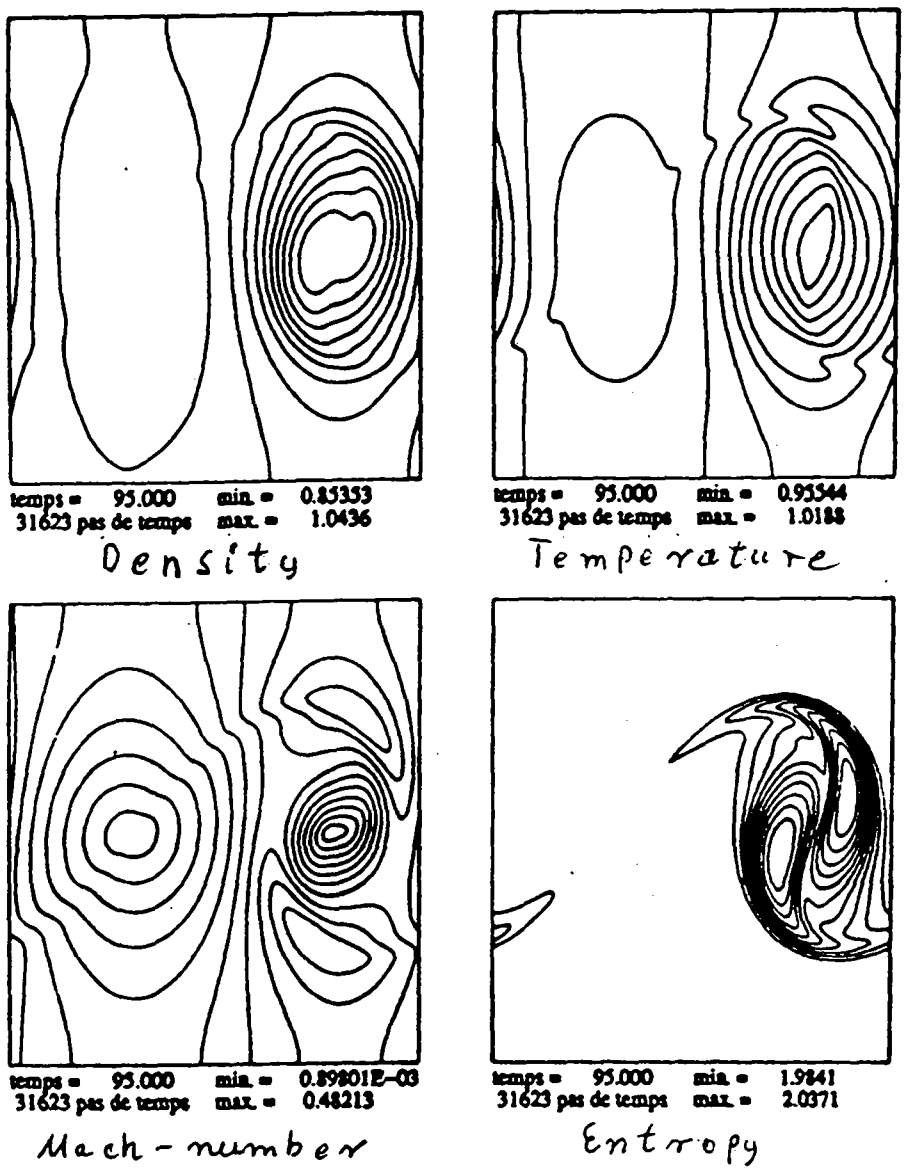

Figure 2: Contour-values of the 2nd order FV-solver, random perturbation, $101 * 101$ grid-points, $Ma_c = 0.3$, $Re = 1000$, $Pr = 0.7$, $L_x = 15.06 \cdot \delta_i$, $t = 95$

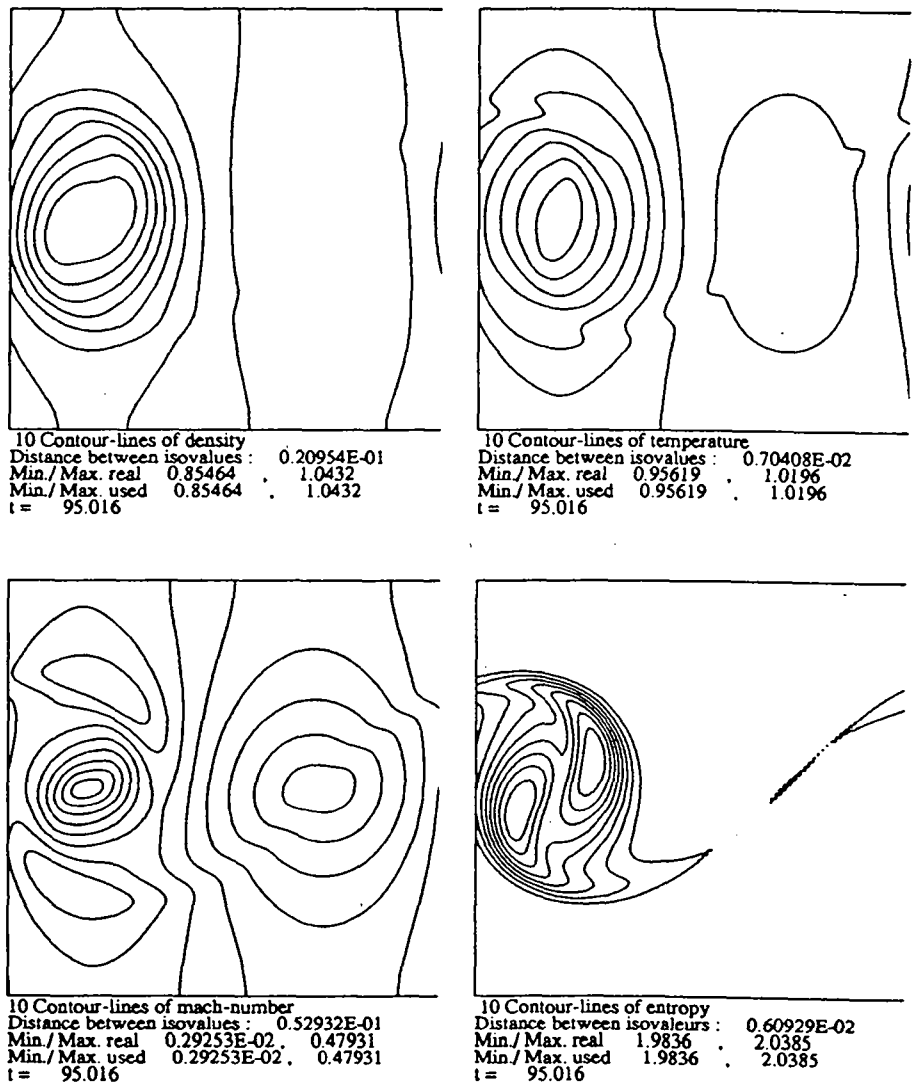

Figure 3: Evolution of vorticity thickness for the random perturbation, $Ma_c = 0.3$, $Re = 1000$, $Pr = 0.7$, $L_x = 15.06\delta_i$

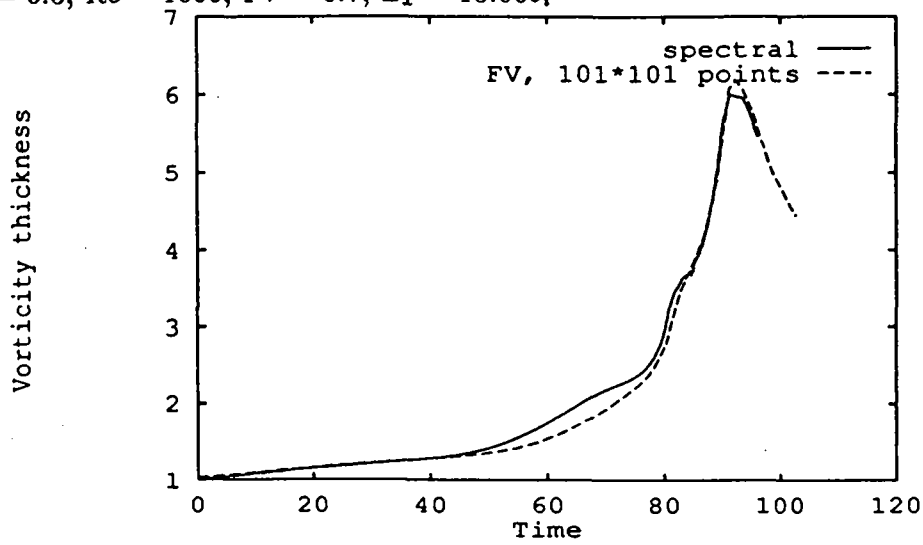

5.2 Test 2: Transonic case

The values of the parameters used for this test are:

$$Ma = 1.6 \quad (i.e. Ma_c = 0.8) \qquad Re = 400 \qquad Pr = 1. \tag{40}$$

$$L_x = 20 \cdot \delta_i \qquad L_y = 10 \cdot \delta_i \qquad \lambda_{pert} = 20 \cdot \delta_i \tag{41}$$

Fig. 4 shows the contour lines of vorticity ω ($\omega = v_x - u_y$), Mach number Ma, temperature T, and vertical velocity v, obtained with the spectral algorithm ($61 * 81$ collocation points) at time $t = 20$. Figure 5 shows the contour-lines of the same quantities obtained with by the second order algorithm with a $101 * 101$ points grid.

One can see that the difference between the contour lines obtained by the two schemes are small. A comparaison of the extreme values of the same quantities, confirms this result. Table 2 shows the extreme values for the two schemes for the time $t = 0$, $t = 20$ and $t = 40$. The difference of the

extreme values of the schemes does not exceed 5 % for all times. Moreover these differences remain approximately constant during the time-integration.

Figure 6 shows the time evolution of the vorticity thickness δ_ω. The error of δ_ω at $t = 0$ is about 5 % for the second order-scheme, while it vanishes for the spectral method.For the time $t = 40$, the difference $\delta_\omega^{spectr.} - \delta_\omega^{fin.vol.}$ is 3.5 %, which is consistent with the value of the difference already observed for the extreme values.

Table 2: Extreme values of the contour-lines for FV-scheme (101 * 101 points) and spectral method (61 * 81 points), deterministic perturbation

$T = 0$

Extreme value	FV-scheme	Spectral method	Difference (%)
T_{max}	1.1280	1.1280	0.0
T_{min}	0.9678	1.0000	3.23
Ma_{max}	0.8831	0.8688	1.65
Ma_{min}	$8.944 \cdot 10^{-10}$	$5.310 \cdot 10^{-15}$	—
ω_{max}	$1.682 \cdot 10^{-2}$	$1.721 \cdot 10^{-2}$	2.26
ω_{min}	-0.9973	-1.0475	4.80

$T = 20$

Extreme value	FV-scheme	Spectral method	Difference (%)
T_{max}	1.1595	1.1569	0.22
T_{min}	0.9719	0.9704	0.15
Ma_{max}	0.9089	0.9039	0.55
Ma_{min}	$4.578 \cdot 10^{-3}$	$2.388 \cdot 10^{-10}$	—
ω_{max}	$1.583 \cdot 10^{-2}$	$1.148 \cdot 10^{-2}$	—
ω_{min}	-0.7291	-0.7412	1.63

$T = 40$

Extreme value	FV-scheme	Spectral method	Difference (%)
T_{max}	1.1553	1.1517	0.003
T_{min}	0.8941	0.9193	2.74
Ma_{max}	1.1043	1.0738	2.84
Ma_{min}	$3.91 \cdot 10^{-3}$	$2.89 \cdot 10^{-4}$	—
ω_{max}	$1.81 \cdot 10^{-2}$	$9.16 \cdot 10^{-3}$	—
ω_{min}	-0.5678	-0.5756	1.36

Figure 4: Contour-values of the spectral method, 61 * 81 collocation points, $Ma_c = 0.8$, $Re = 400$, $Pr = 0.7$, $L_x = 20\delta_i$, $t = 20$

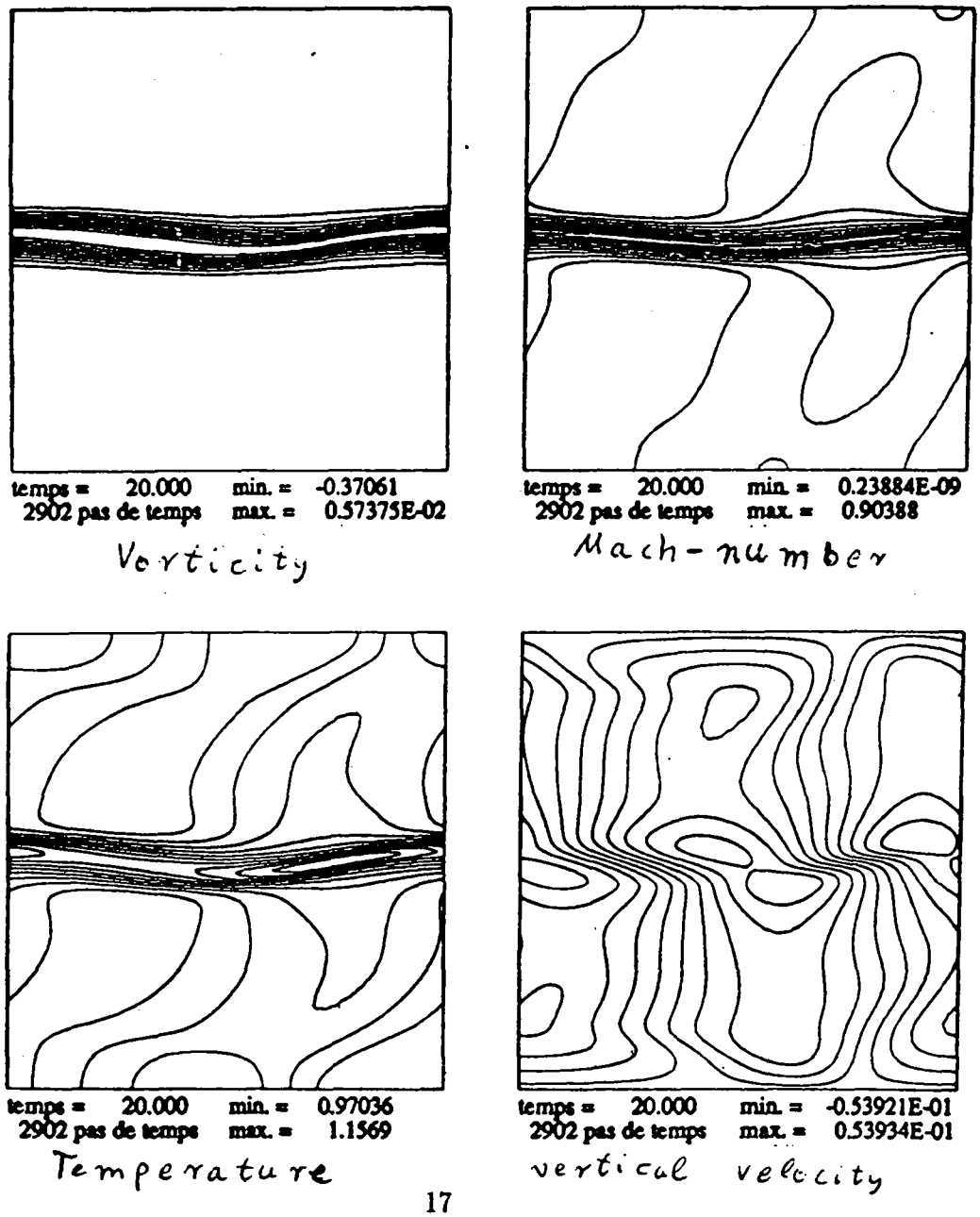

Figure 5: Contour-values of the 2nd order FV-solver, 101 * 101 grid-points, $Ma_c = 0.8$, $Re = 400$, $Pr = 0.7$, $L_x = 20\delta_i$, $t = 20$

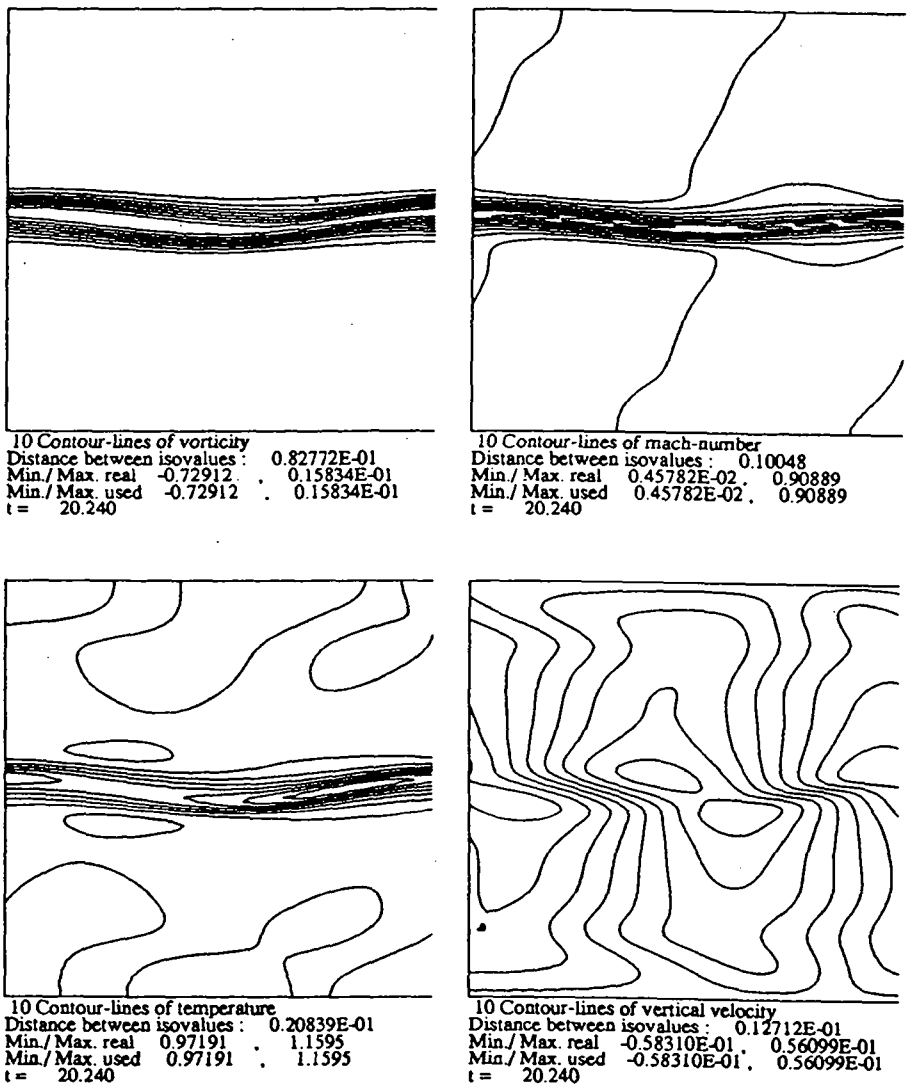

Figure 6: δ_ω as function of time, $Ma_c = 0.8$, $Re = 400$, $Pr = 1.0$, $L_x = 20 \cdot \delta_i$

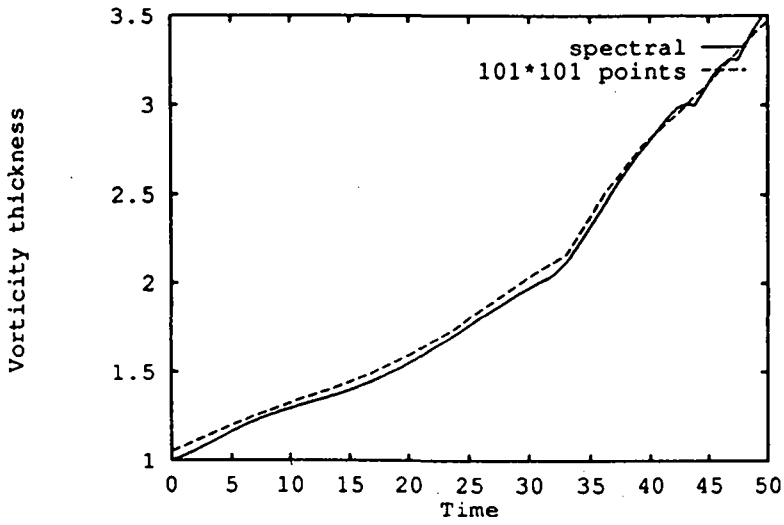

6 Simulations with shocks

In this section we will report four test-cases where shocks appear. No high-resolution (i.e spectral) results exist for these test cases, therefore we check the accuracy of the solution by increasing the number of grid-points and grid-free solutions are researched.The first test simply consists in the continuation of the last test-case of the preceeding section. We will then report three simulations where pairing-events occur. Two simulations with two structures, resulting from a deterministic and a random perturbation, will be shown. Finally we end with a four-structure simulation where the effect of the initial growth of the layer due to physical viscosity is discussed.

6.1 Simulation with one structure

This computation is just the continuation of the preceeding computation, so the parameters of the simulation are :

$$Ma = 1.6 \ \ (i.e. Ma_c = 0.8), \qquad Re = 400, \qquad Pr = 0.7, \tag{42}$$

$$L_x = 20 \cdot \delta_i, \qquad L_y = 10 \cdot \delta_i \qquad \lambda_{pert} = 20 \cdot \delta_i$$

Fig. 7 shows the evolution of the vorticity-thickness as function of time for two different numbers of grid-points in the x-direction. The differences between both curves are really small, they do not exeed 1.5 %.

Figure 7: Evolution of vorticity thickness as function of Time: $Ma_c = 0.8$, $Re = 400$, $Pr = 0.7$, $L_x = 20 \cdot \delta_i$

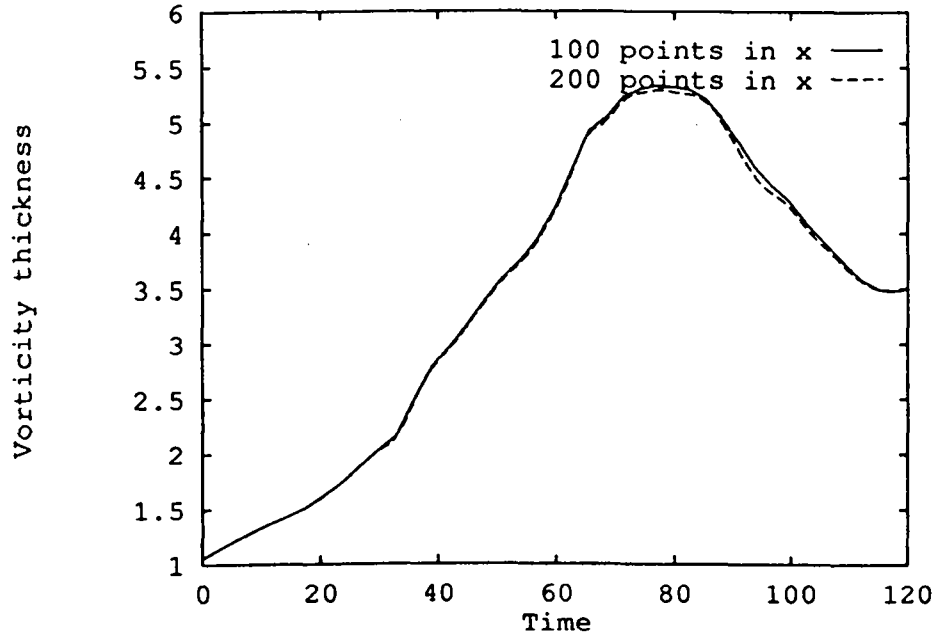

Fig 8 shows the contour-lines of density ρ, temperature T, Mach number Ma, and entropy S at the time $t = 80$ with 101 points in x-direction. Fig. 9 shows the same contour lines, but with a resolution of 201 points in x. In both figures, the shock and the vortex can clearly be seen. Evidently, in the high-resolution solution, the shocks are much sharper than in the low-resolution one. However, although the shape of the contour-lines does not differ much, the corresponding extreme-values show a difference of about 10 % (table 3). This suggests that in the details, the results are not really grid-converged. This point is further studied in the following section.

Figure 8: Contour-lines with 101 points in x-direction, $Ma_c = 0.8$, $Re = 400$, $Pr = 0.7$, $L_x = 20 \cdot \delta_i$, $t = 80$

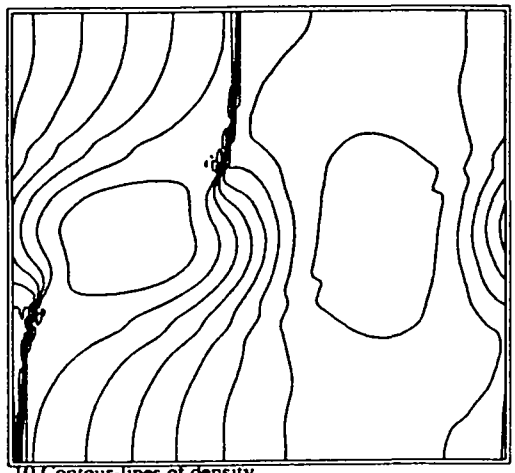

10 Contour-lines of density
Distance between isovalues : 0.95056E-01
Min./ Max. real 0.49104 . 1.3465
Min./ Max. used 0.49104 . 1.3465
t = 80.023

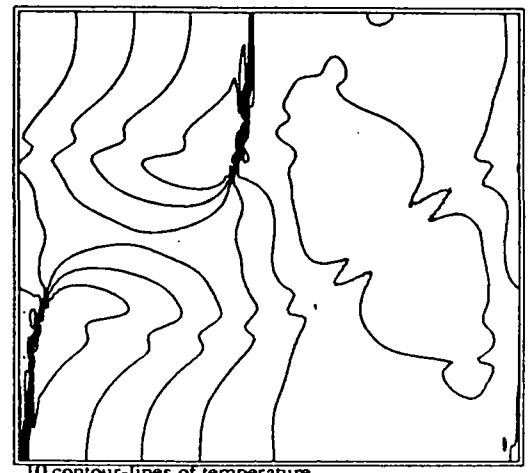

10 contour-lines of temperature
Distance between contour-lines : 0.49593E-01
Min./ Max. real 0.69963 . 1.1460
Min./ Max. used 0.69963 . 1.1460
t = 80.023

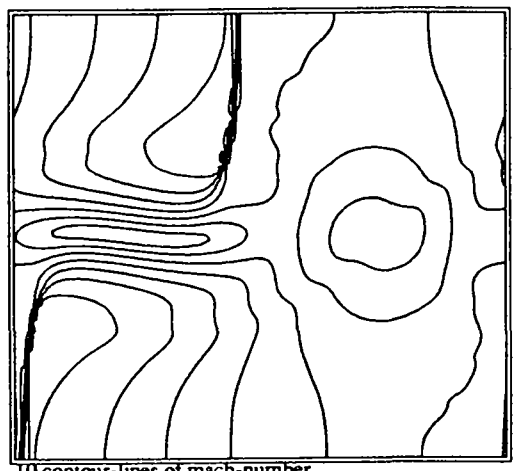

10 contour-lines of mach-number
Distance between contour-lines: 0.18618
Min./ Max. real 0.39357E-02 . 1.6795
Min./ Max. used 0.39357E-02 . 1.6795
t = 80.023

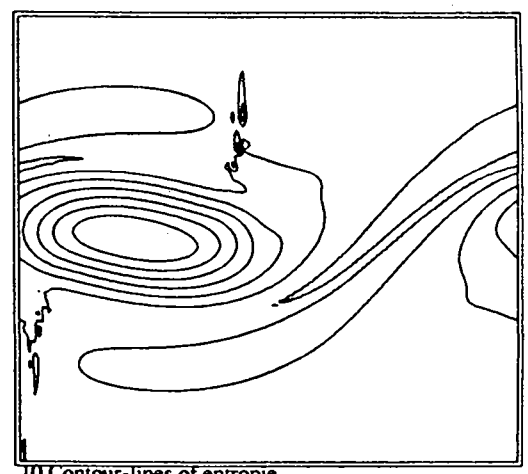

10 Contour-lines of entropie
Distance between contour-lines : 0.10643E-01
Min./ Max. real 0.25656 . 0.35235
Min./ Max. used 0.25656 . 0.35235
t = 80.023

Figure 9: Contour-lines with 201 points in x-direction, $Ma_c = 0.8$, $Re = 400$, $Pr = 0.7$, $L_x = 20 \cdot \delta_i$, $t = 80$

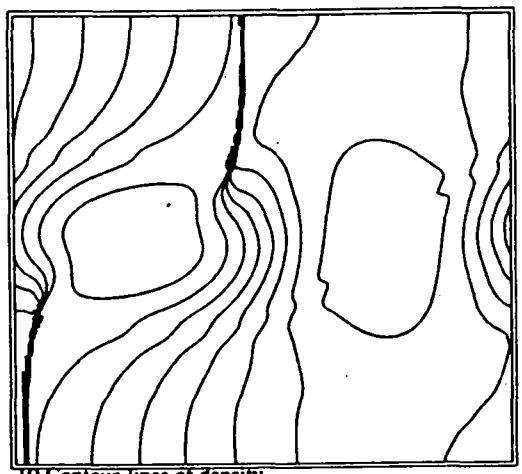

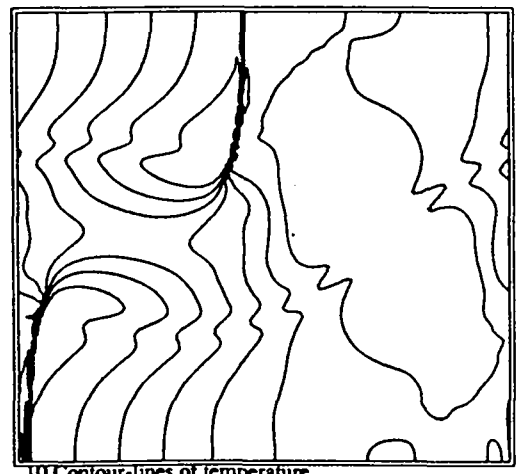

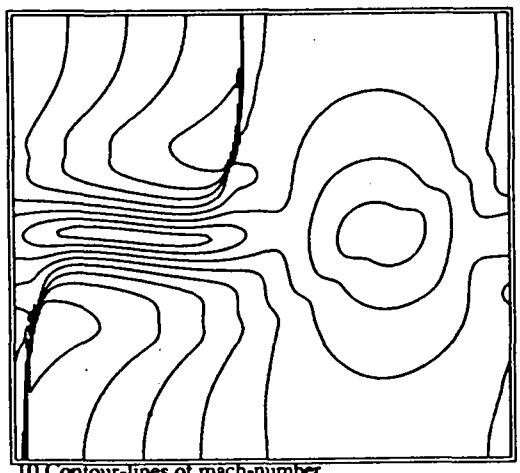

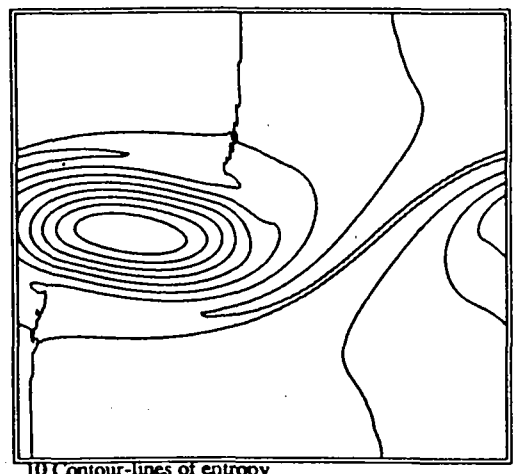

Table 3: Comparaison of extreme-values of the contour-lines, Ma=0.8, Re=400, Pr=0.7, 101 points in y

extreme-value	101 points	201 points	Difference (%)
ρ_{min}	0.4910	0.4922	0.1
ρ_{max}	1.3465	1.3479	0.1
T_{min}	0.6996	0.7671	8.8
T_{max}	1.1460	1.1304	1.4
Ma_{min}	$3.9 \cdot 10^{-3}$	$2.8 \cdot 10^{-3}$	—
Ma_{max}	1.6795	1.5253	10.1

Energy-spectra:

Fig. 10 shows the energy-spectra at the times $t = 40$ and $t = 80$, with 101 and 201 points in x-direction. The abscissa corresponds to a normalized wavenumber $l = \frac{L_x}{2\pi}k$. Thus $l = 1$ corresponds to a perturbation with a wavelength the x-dimension of the domain. The growth of the vortex is reflected by a growth of the amplitude $l = 1$ between $t = 40$ and $t = 80$.

The high wavenumber range of the spectrum at $t = 40$ decreases to $e(k) = 10^{-13}$, so that there is no energy left in the high-k-range. This, and the fact that there are negligible differences between the spectrum obtained with 101- and 201 points, suggest that shock-free flow with one structure is well represented with 101 points.

At time $t = 80$ shocks appear, so that small structures have to be resolved. This is reflected by a slower decrease of the spectrum than at $t = 40$. Moreover in the high wavenumber range, differences between the 101- and 200-point computations begin to appear for $l > 20$ corresponding to a structure of typical size less than $\frac{L_x}{20}$ (i. e. $5\Delta x$ for the low resolution run). Note also, that the 201 -point spectrum decreases only by one decade with respect to the 101-point spectrum and that the two spectra develop a plateau in the high wavenumber range. Using the Helmholtz decomposition, we now investigate if this results only from the emergence of shocks, or if the "incompressible" part of the flow also possesses unresolved fine structures.

Figure 10: Energy-spectra, $t = 40$ and $t = 80$, $Ma_c = 0.8$, $Re = 400$, $Pr = 0.7$, $L_x = 20 \cdot \delta_i$

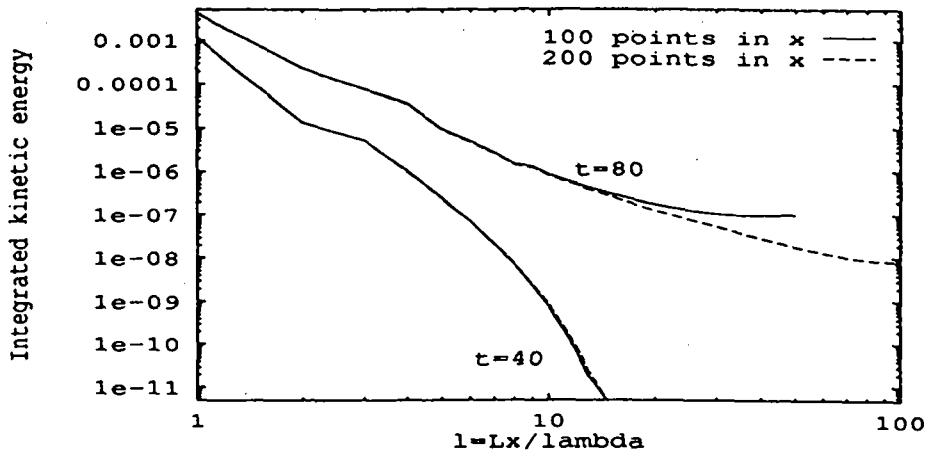

Separation of the flow-field:
The flow-field $\vec{u}$ is separated into

$$\vec{u} = \vec{u_i} + \vec{u_c} \tag{43}$$

$$\begin{bmatrix} u \\ v \end{bmatrix} = \begin{bmatrix} u_i \\ v_i \end{bmatrix} + \begin{bmatrix} u_c \\ v_c \end{bmatrix} \tag{44}$$

Fig. 12 shows on the left hand side the horizontal component of the "compressible" part of the flow-field u_c at the Time $t = 80$. On the right-hand-side, the horizontal component of the "incompressible" part of the flow-field is shown. The resolution is 201 points in x-direction and 101 points in y-direction. In the left-hand-side, the shock appears, but there are no vortical structures left, while in the right figure the vortex can clearly be seen and only a small rest of the shock comes up. By comparing with Fig. 11 that shows the velocity field at the same time, it can be seen that the Helmholtz decomposition is quite effective in splitting the "incompressible" part of the flow from the "compressible" one.

Figure 11: Contour-lines of u, 201 points in x-direction

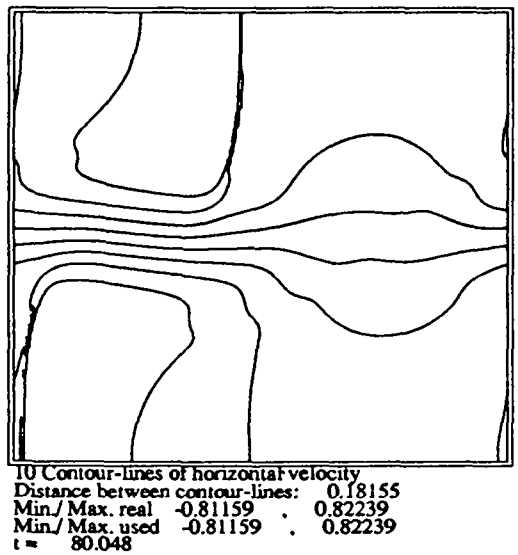

Figure 12: Contour-lines of u_c (left) and u_i (right), 201 points in x-direction

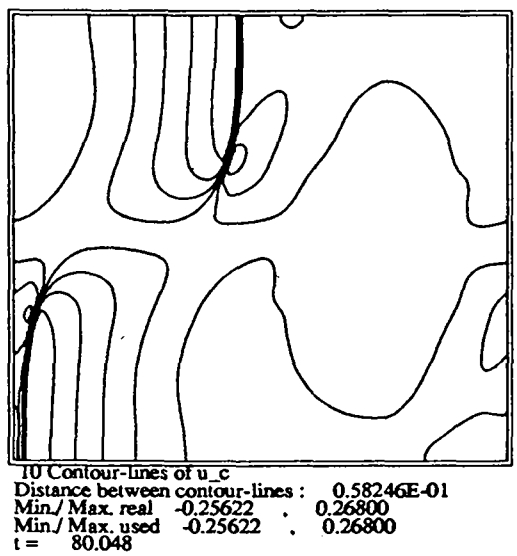

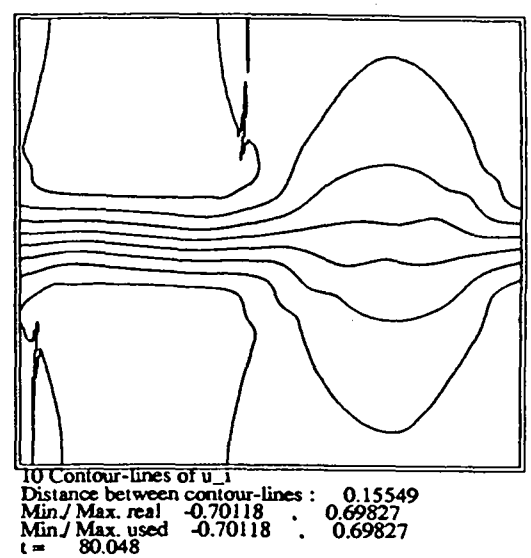

Spectra of u_c and u_i:

Fig. 13 shows the spectra of the integrated kinetic energy of the compressible part of the flow-field, while fig. 14 shows the corresponding spectrum of the incompressible part of the flow-field. Again, the structure of wavelength $\lambda = 20$ is represented in both spectra as a maximum at $l = \frac{L_x}{\lambda} = 1$. Note that the more energetic structures are concentrated in the "incompressible" part of the flow field, where the amplitude of the $l = 1$ mode is roughly 10 times larger than in the "compressible" part.

At time $t = 40$, the spectra of $\vec{u_c}$ and $\vec{u_i}$ decrease with roughly the same slope to $e(k) = 10^{-12}$. The differences beween the 101 and 201 points runs are negligible and concentrated in the "compressible" part of the velocity field. This again confirms that the flow-field at $t = 40$ is well resolved.

At time $T = 80$, the vortical structure has grown inducing the emergence of shocks in the flow field. It can be seen on fig. 13 and 14 that the growth of the amplitude of the first mode corresponding to $l = 1$ is almost exclusively concentrated in the "incompressible" part of the flow. Moreover, the slope of the " incompressible" spectrum is roughly the same between $t = 40$ and $t = 80$ for the low wavenumber part of the spectrum. On the contrary, the spectrum of the "compressible" part of the velocity field shows a change of slope reflecting the appearance of shocks. However no noticeable differences can be seen in the "compressible" spectrum between the 101 and 201 points runs and surprisingly it is in the high wavenumber part of the "incompressible" spectrum that differences appear. Actually comparing fig. 10 and 14 it can be seen that the appearance of a plateau for $l > 20$ in fig. 10 is due to a rise of the energy of the high wavenumber mode of the "incompressible" part of the flow. This suggests that independently of the shock emergence, there are some structures that are not totally well resolved even with a 201 point grid, however the differences are small and this can be considered as marginal.

Figure 13: Spectrum of the compressible part of the flow-field ($\vec{u_c}$), 101 and 201 points in x-direction

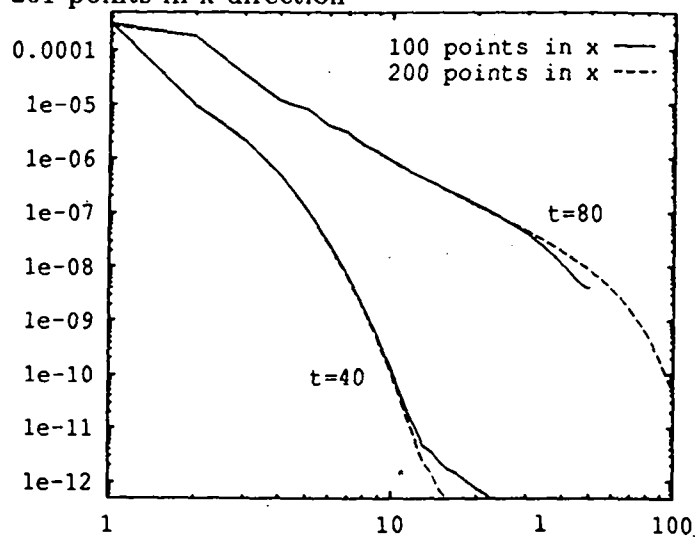

Figure 14: Spectrum of the incompressible part of the flow-field ($\vec{u_i}$), 101 and 201 points in x-direction

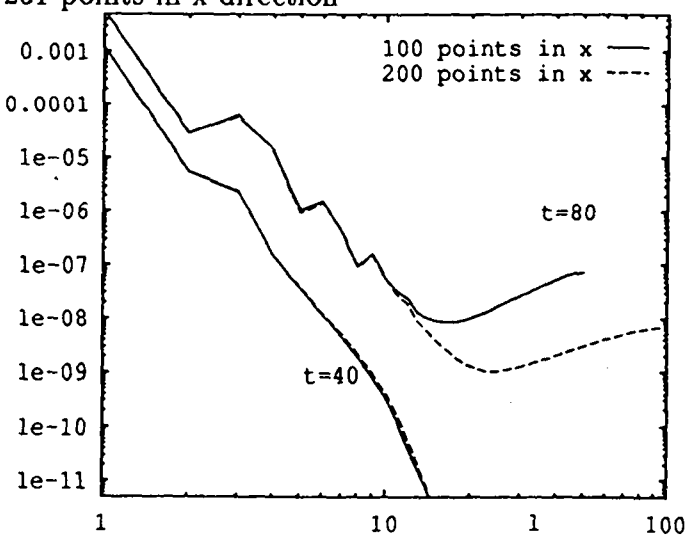

6.2 Simulation with two structures: deterministic perturbation

In the first part of this study (section 5) we have shown by a comparaison of the results obtained with a spectral method, that a subsonic ($Ma_c = 0.3$) two-structure computation leading to a pairing event, can adequately be computed with a low resolution ($101 * 101$ points) grid. Here, we investigate these two-structure computations for larger convective Mach numbers when shocks appear. The parameters for this computations are

$$Ma = 1.6 \ \ (i.e. Ma_c = 0.8), \qquad Re = 1000, \qquad Pr = 0.7 \tag{45}$$
$$L_x = 22.52 \cdot \delta_i \qquad L_y = 22.52 \cdot \delta_i \qquad \lambda_{pert} = 11.26 \cdot \delta_i$$

The deterministic perturbation used is defined by:

$$u' = \frac{\varepsilon \cdot y \cdot \lambda_{pert}}{20 \cdot \pi} \sin\left(\frac{2\pi}{\lambda_{pert}}(x - \frac{\lambda_{pert}}{5})\right) \cdot \exp(-\frac{1}{10}y^2) \tag{46}$$

$$v' = \frac{\varepsilon}{2} cos\left(\frac{2\pi}{\lambda_{pert}}(x - \frac{\lambda_{pert}}{5})\right) \cdot \exp(-\frac{1}{10}y^2) \tag{47}$$

where the factor $(x - \frac{\lambda_{pert}}{5})$ is used to shift the flow field in order to obtain shocks in the centre of the computational domain. The amplitude ε of the perturbation is $\varepsilon = 0.1$. The length of the box corresponds to two-times the wave-length of the most amplified perturbation according to inviscid stability theory. The grid is a cartesian grid, equidistant in x-direction, and stretched in y-direction. The stretching in y-direction is obtained by a transformation of co-ordinates:

$$y_1 = -1 + \frac{2}{N_y} \tag{48}$$

$$y = L_y[(1 - \alpha) \cdot y_1^3 + \alpha \cdot y_1] \tag{49}$$

The parameter α determines the stretching of the grid. In this simulation, $\alpha = 0.5$ was used. The number of grid-points in x-direction varied from $N_x = 101$ to $N_x = 401$ points, while in y-direction $Ny = 101$ points were used.

Fig. 15 shows the evolution of the vorticity-thickness δ_ω in time with three

different resolutions. The shapes of the curves are roughly the same. The first maximum at $t \simeq 60$ corresponds to the emergence of two structures, while the minimum at $t \simeq 120$ corresponds to the beginning of the pairing process. Up to the time $t = 120$ the differences between the solutions are small. For times $t > 120$ one observes that the high-resolution solutions show a slower development than the low-resolution ones.

A compararison of the contour-lines confirmes the influence of the number of grid-points for larger times. Up to $t = 120$ (fig. 16 and 17), the contour-lines do not show big differences. Table 4 shows that these differences do not exceed 10 %

But for the time $t = 180$ (fig. 18), the differences are important. One observes that the strength of the shock is decreasing with an increasing number of grid-points in x-direction. In the solution with 401 points in x, the shock nearly disappeares. Table 4 shows a constant decrease of the maximum Mach number with an increasing number of points in x-direction. The other extreme-values show differences of up to 25 %. Also the shape of the contour-lines is not the same. In the high-resolution solution, the vortices are thinner than in the low-resolution one. This can be explained by the slower development of the high-resolution solution. These results show, that even with 401 points in the x-direction, the solution is not grid-free for $t > 120$.

We have also noted that these differences results from spatial error and that the temporal error is not significant for these computations : As an explicit time integration is used, the time step depends upon the number of grid points and therefore one may suspect that the value of the time step has an influence on the accuracy of the different computations. However, by using the same time step in the low-resolution runs than in the high-resolution one, we have checked that the differences persist.

Figure 15: Evolution of vorticity-thickness as function of time, $Ma_c = 0.8$, $Re = 1000$, $Pr = 0.7$, $L_x = 22.52 \cdot \delta_i$

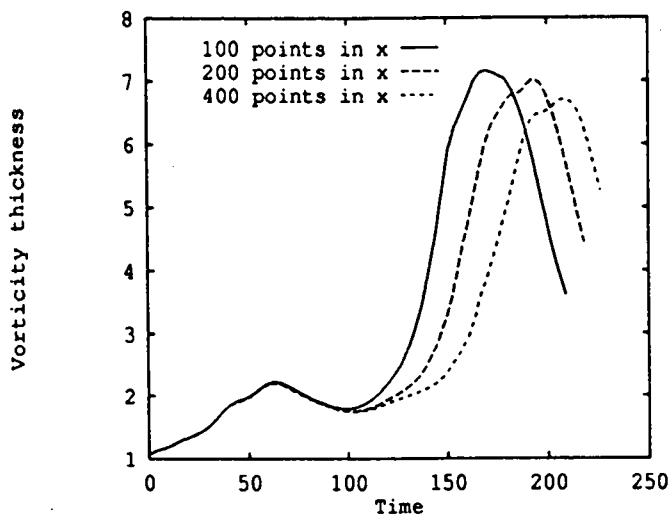

Figure 16: Contour-lines of entropy with 101 points (left) and 401 points (right), $Ma_c = 0.8$, $Re = 1000$, $Pr = 0.7$, $L_x = 22.52 \cdot \delta_i$, $t = 60$

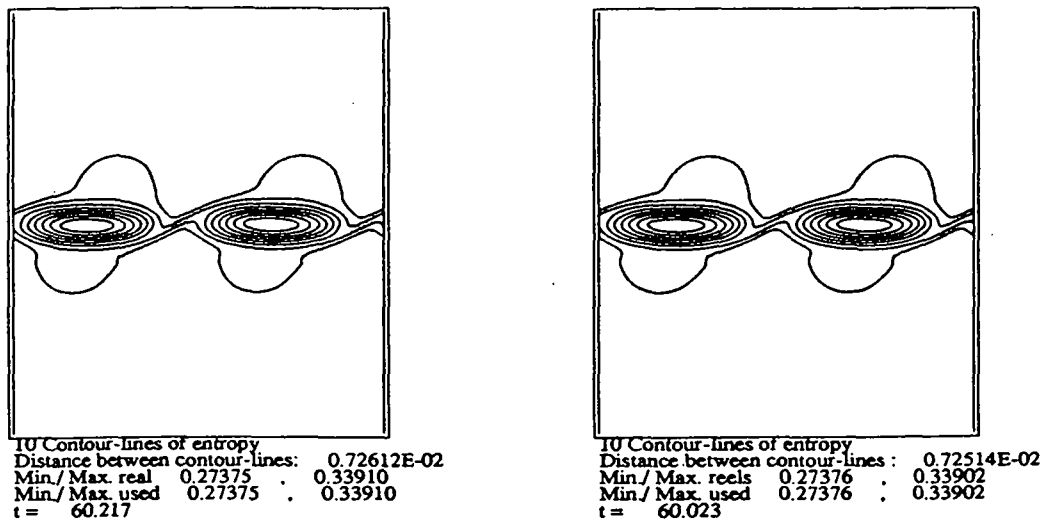

Figure 17: Contour-lines of entropy with 101 points (left) and 401 points (right), $Ma_c = 0.8$, $Re = 1000$, $Pr = 0.7$, $L_x = 22.52 \cdot \delta_i$, $t = 120$

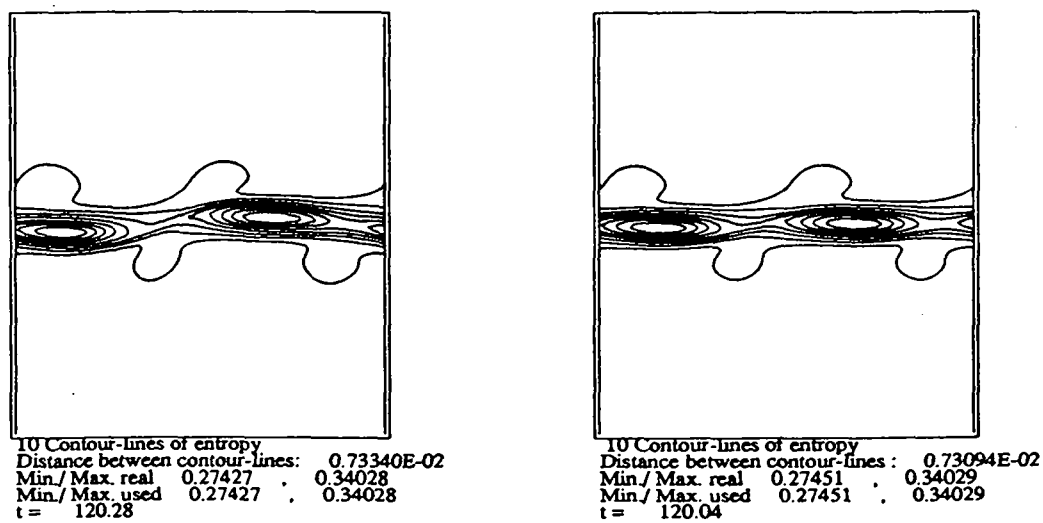

Figure 18: Contour-lines with 101 points, $Ma_c = 0.8$, $Re = 1000$, $Pr = 0.7$
$L_x = 22.52 \cdot \delta_i$, $T = 180$

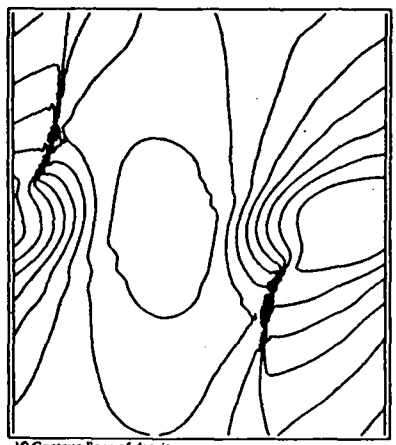

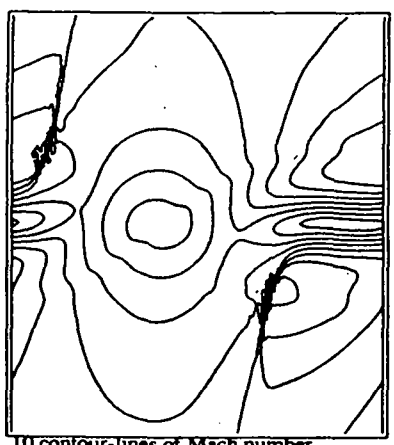

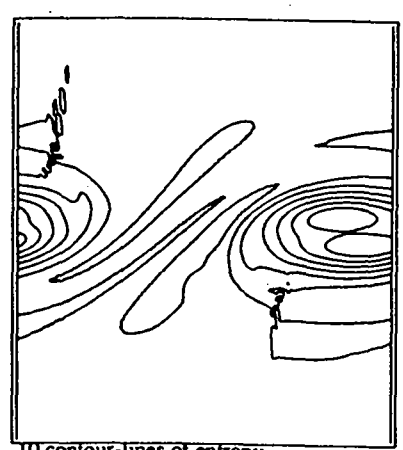

Figure 19: Contour-lines with 401 points, $Ma_c = 0.8$, $Re = 1000$, $Pr = 0.7$, $L_x = 22.52 \cdot \delta_i$, $T = 180$

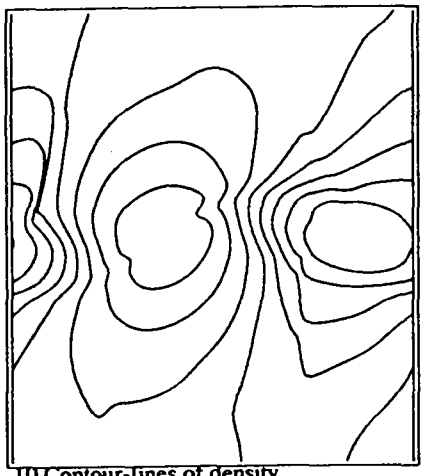

10 Contour-lines of density
Distance between contour-lines : 0.88460E-01
Min./ Max. real 0.54727 . 1.3434
Min./ Max. used 0.54727 . 1.3434
t = 180.06

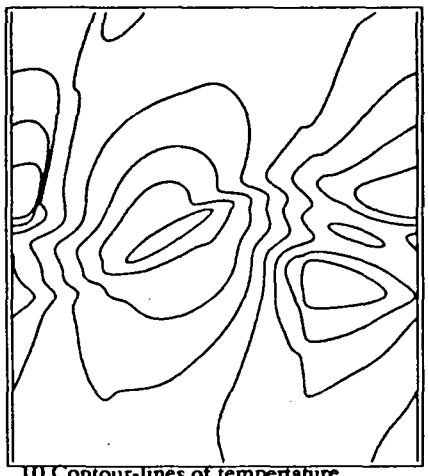

10 Contour-lines of tempertature
Distance between contour-lines : 0.33602E-01
Min./ Max. real 0.86743 . 1.1699
Min./ Max. used 0.86743 . 1.1699
t = 180.06

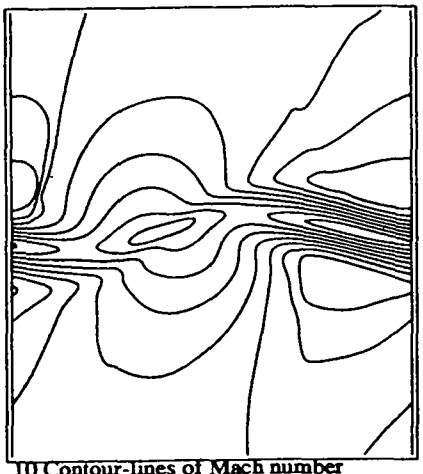

10 Contour-lines of Mach number
Distance between contour-lines : 0.13597
Min./ Max. real 0.56293E-02 . 1.2294
Min./ Max. used 0.56293E-02 . 1.2294
t = 180.06

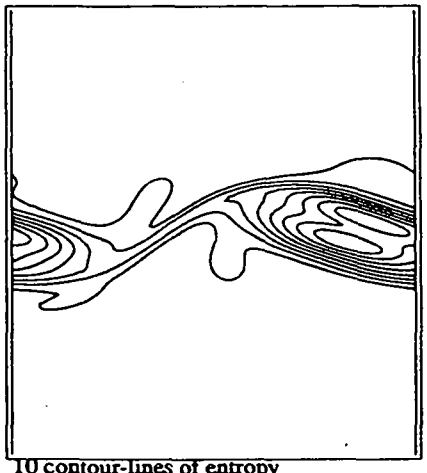

10 contour-lines of entropy
Distance between contour-lines : 0.69132E-02
Min./ Max. real 0.27477 . 0.33699
Min./ Max. used 0.27477 . 0.33699
t = 180.06

Table 4: Extreme-values of the contour-lines, 101, 201 and 401 points in x-direction, 101 points in y-direction

extreme-value	101 points	201 points	401 points	Difference 101-401 points(%)
$T = 60$				
ρ_{min}	0.6440	0.6469	0.6484	0.7
ρ_{max}	1.2778	1.2748	1.2726	0.4
T_{min}	0.9220	0.9231	0.9238	0.2
T_{max}	1.1476	1.1475	1.1487	0.1
Ma_{min}	$1.6 \cdot 10^{-2}$	$1.7 \cdot 10^{-3}$	$1.6 \cdot 10^{-2}$	—
Ma_{max}	1.1147	1.1113	1.1088	0.5
$T = 120$				
ρ_{min}	0.7383	0.7531	0.7568	2.4
ρ_{max}	1.2015	1.1457	1.1175	7.5
T_{min}	0.9557	0.9583	0.9591	0.3
T_{max}	1.1529	1.1409	1.1342	1.6
Ma_{min}	$3 \cdot 10^{-3}$	10^{-2}	10^{-2}	—
Ma_{max}	0.9835	0.9543	0.9410	4.5
$T = 180$				
ρ_{min}	0.4378	0.4890	0.5473	20.0
ρ_{max}	1.2965	1.3361	1.3434	3.5
T_{min}	0.7552	0.7697	0.8674	12.9
T_{max}	1.1323	1.1438	1.1699	3.2
Ma_{min}	$2 \cdot 10^{-3}$	$6 \cdot 10^{-3}$	$6 \cdot 10^{-3}$	—
Ma_{max}	1.5438	1.4749	1.2294	25.6

Energy-spectra:

Fig. 20 shows the energy-spectra at the time $t = 120$ with 101 and 401 points in x. The most striking difference between the two results is the damping of all odd modes in the 401-point run with respect to the 101-point result. For instance, while the fundamental mode (two structures with $\lambda_{pert} = 11.26$) can be seen as a peak at $l = 2$, of approximately the same magnitude in the two computations, the first subharmonic mode, represented as a peak at $l = 1$, possesses considerably less energy in the highly resolved computation. The same results can be seen for all the modes up to $l = 10$: while the even modes are approximately the same in the two computations, the odd modes are less energetic in the 401-points computation. Because pairing results essentially from an interaction of the fundamental and its first subharmonic, this explains why a slower development of the mixing process is obtained for the best resolved computation. Note, that Atkins [1], has also observed that spurious generation of the subharmonic mode can be produced by second-order TVD-schemes.

Figure 20: Spectrum of integrated kinetic energy, $Ma_c = 0.8$, $Re = 1000$, $Pr = 0.7$, $L_x = 22.52 \cdot \delta_i$

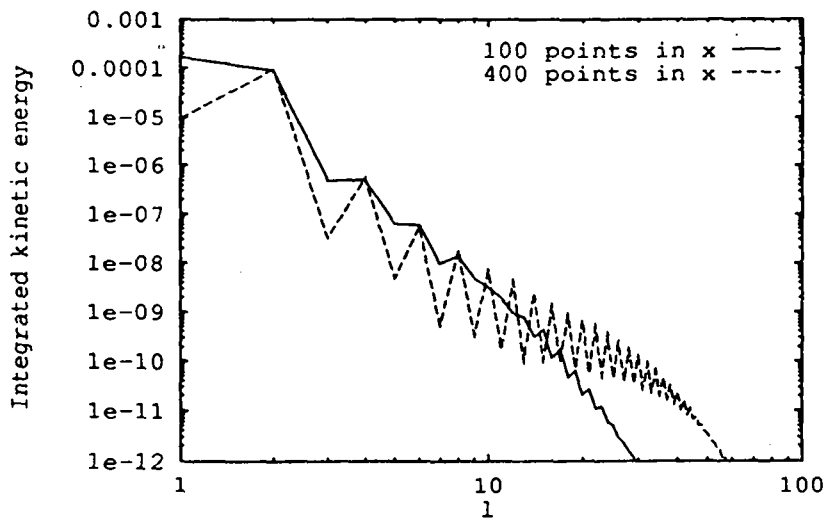

Decomposition of the flow-field:

Fig. 21 shows the horizontal component of the compressible part of the flow-field u_c, fig. 22 shows the horizontal component of the incompressible part of the flow-field u_i at the time $t = 120$. Fig. 23 and 24 show the same quantities at the time $t = 180$. The small amplitude of the "compressible" part of the velocity-field ($\pm 10^{-2}$) at $t = 120$ indicates that the flow behaves almost like an incompressible one at this $t = 120$. But there is a considerable increase of the amplitude (roughly a factor 10) of the "compressible" part of the velocity-field between $t = 120$ and $t = 180$.

Note that in fig. 22 the differences between the 101 and 401 points solution are now qualitatively important. The deformation of the shear-layer in the 101-point-solution is more developed than in the 401-point-solution, and while the extreme values of the "incompressible part" are of same order, there is almost a factor two in the extreme value of the "compressible part" at time $t = 180$.

Figure 21: Contour-lines of u_c: 101 points in x (left), 401 points in x (right), t=120

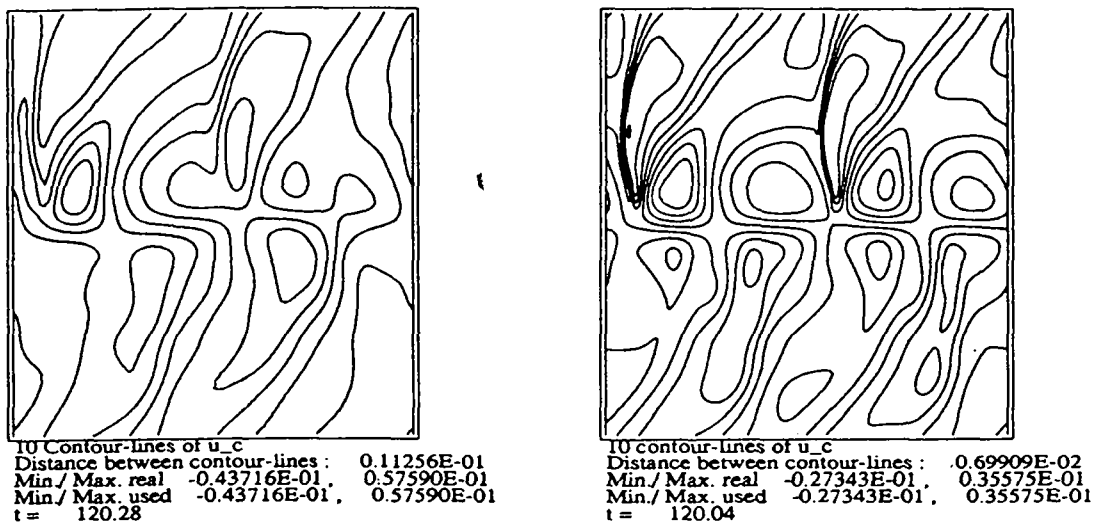

Figure 22: Contour-lines of u_i: 101 points in x (left), 401 points in x (right), t=120

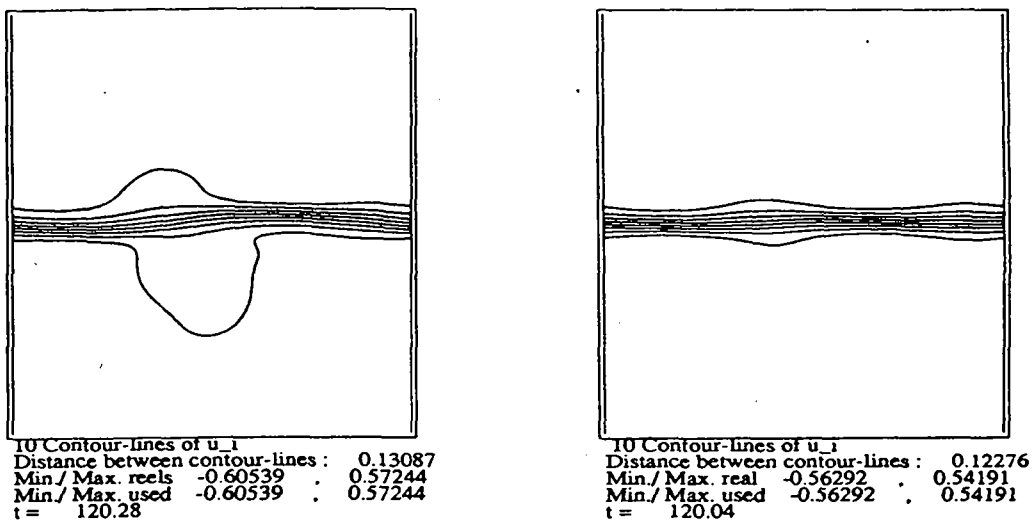

Figure 23: Contour-lines of u_c: 101 points in x (left), 401 points in x (right), t=180

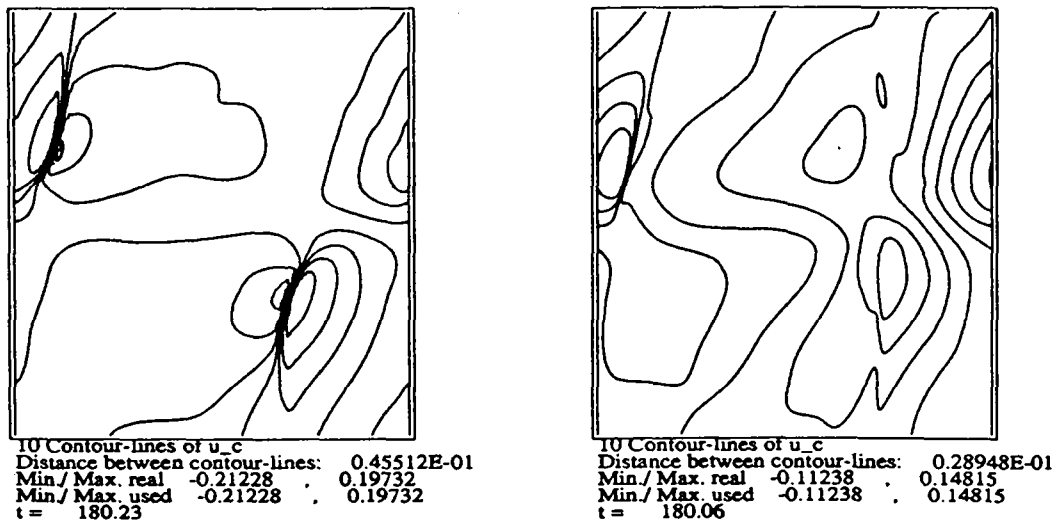

Figure 24: Contour-lines of u_i: 101 points in x (left), 401 points in x (right), t=180

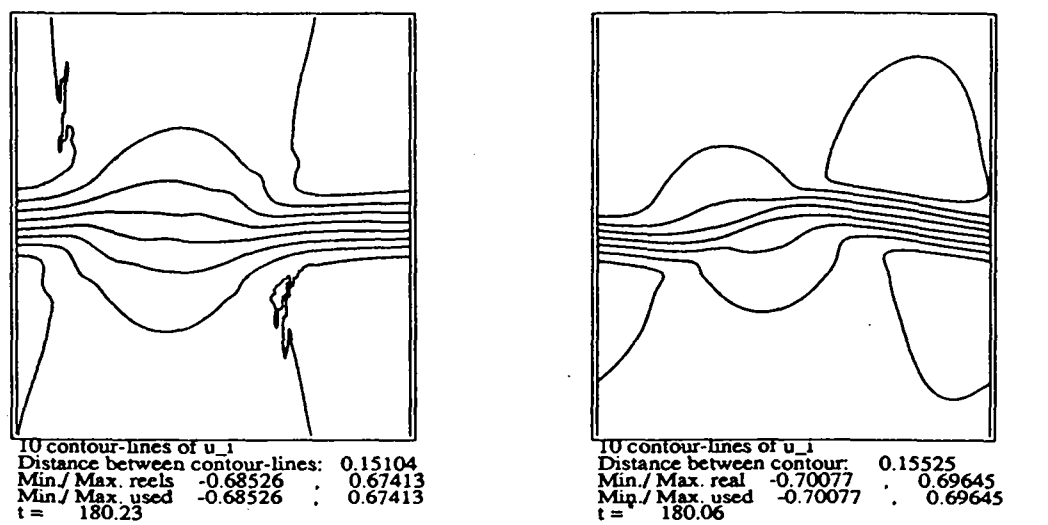

Spectra of u_c and u_i:

Fig. 25 shows the spectrum of the integrated kinetic energy of the "compressible part" of the flow-field $\vec{u_c}$, fig. 26 the one of the "incompressible part" $\vec{u_i}$. In these spectra the coherent structures are represented as peaks at $l = \frac{L_x}{\lambda} = 1$ and $l = 2$. Again the most striking difference between the spectra obtained with 101 points and the one obtained with 401 points are the oscillations, which appear in the 401 points spectrum. The even modes seem to be more amplified than the odd ones. Also, the 101-points spectrum decreases faster to 10^{-14} than the 401-points spectrum.

Figure 25: Spectrum of integrated kinetic energy of u_c, $Ma_c = 0.8$, $Re = 1000$, $Pr = 0.7$, $L_x = 22.52 \cdot \delta_i$

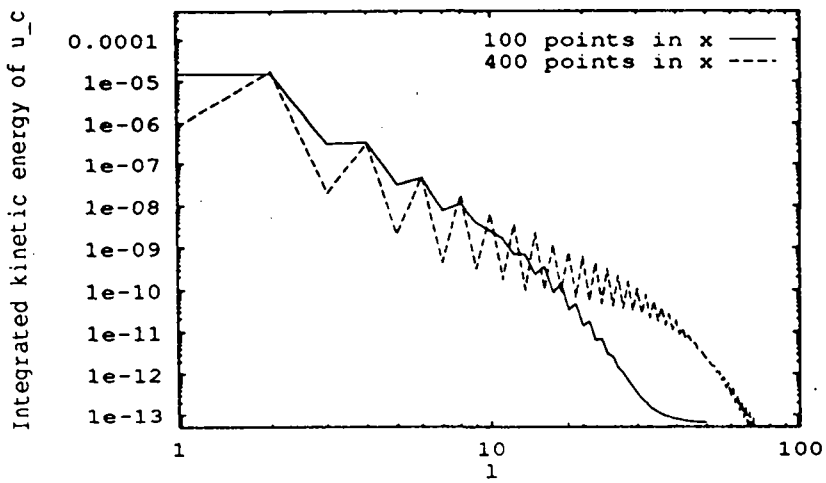

Figure 26: Spectrum of integrated kinetic energy of u_i, $Ma_c = 0.8$, $Re = 1000$, $Pr = 0.7$, $L_x = 22.52 \cdot \delta_i$

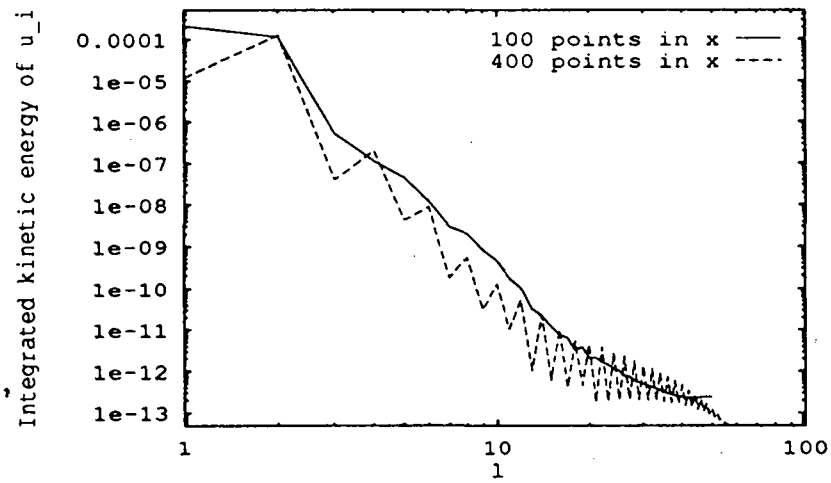

6.3 Simulations with two structures: random perturbation

The values of the parameters used for this computation are

$$Ma = 1.6 \quad (i.e. Ma_c = 0.8) \qquad Re = 1000 \qquad Pr = 0.7 \tag{50}$$

$$L_x = 45.04 \cdot \delta_i \qquad L_y = 11.26 \cdot \delta_i \tag{51}$$

The grid is an equidistant grid in x- as well as in y-direction. The number of grid-points varies from $N_x = 101$ to $N_x = 401$ points in x-direction, while in y-direction $N_y = 101$points are used. The perturbation is the random perturbation, given by eq. (14) (15). The box length is four times the wavelength of the most amplified perturbation according to linear inviscid analysis of stability. So there should appear four vortices in the simulation. But in fig. 27 and 28 only two vortices appear. This is due to a self-stabilizing effect of the physical viscosity. This effect will be explained in the next section.

Fig. 27 shows the contour lines of density ρ, temperature T, Mach number Ma, and entropy S at time $T = 250$ and $T = 330$, obtained with a $101 * 101$ points grid. Fig. 28 shows the same computation on a $401 * 101$ points grid, so the numerical resolution in x-direction in fig 28 is four times better than in fig. 27.
Of course, the shocks in the high-resolution computations are sharper than those in the low-resolution ones. A comparaison of the extreme values of the contour lines shows differences of up to 11 % (Tab 5). Fig. 29 shows the evolution of the vorticity thickness for both computations. One sees that the vorticity thickness of the high-resolution computation develops much faster than the low-resolution one. A comparaison of the contour lines confirms this result. For time $T = 250$ figures 27 and 28 show two separated vortices. At $t = 330$ in the low-resolution computation the vortices are aligning for vortex pairing, while in the high-resolution computation the vortex pairing is already done.

Figure 27: Contour lines of two-structure-computation for two times, t=250 and t=330, 101 * 101 grid points, $Ma_c = 0.8$, $Re = 1000$, $Pr = 0.7$, $L_x = 45.04 \cdot \delta_i$, random perturbation

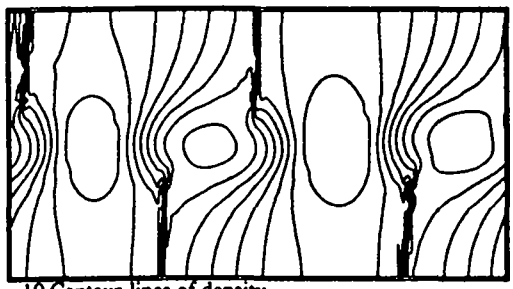

10 Contour-lines of density
Distance between isovalues : 0.96934E-01
Min./ Max. real 0.49064 , 1.3631
Min./ Max. used 0.49064 , 1.3631
t = 250.24

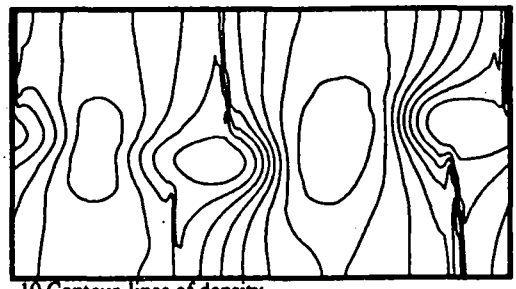

10 Contour-lines of density
Distance between isovalues : 0.88252E-01
Min./ Max. reels 0.59448 , 1.3887
Min./ Max. used 0.59448 , 1.3887
t = 330.01

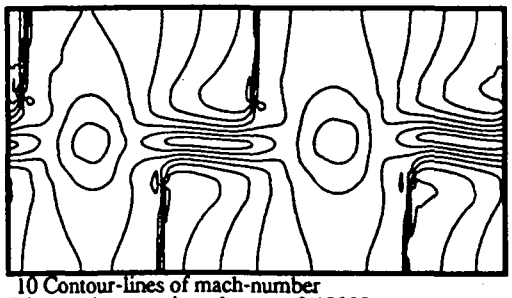

10 Contour-lines of mach-number
Distance between isovalues : 0.19229
Min./ Max. real 0.52325E-02 , 1.7359
Min./ Max. used 0.52325E-02 , 1.7359
t = 250.24

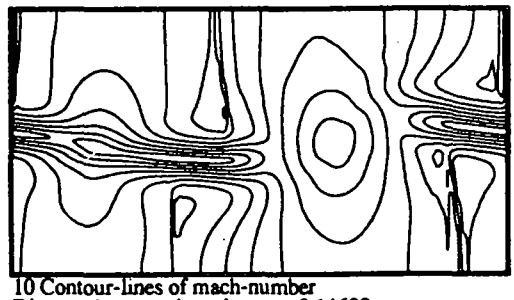

10 Contour-lines of mach-number
Distance between isovalues : 0.14608
Min./ Max. real 0.15779E-01 , 1.3305
Min./ Max. used 0.15779E-01 , 1.3305
t = 330.01

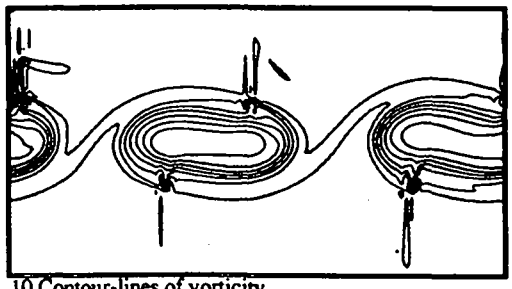

10 Contour-lines of vorticity
Distance between isovalues : 0.48730E-01
Min./ Max. reels -0.35236 , 0.86207E-01
Min./ Max. used -0.35236 , 0.86207E-01
t = 250.24

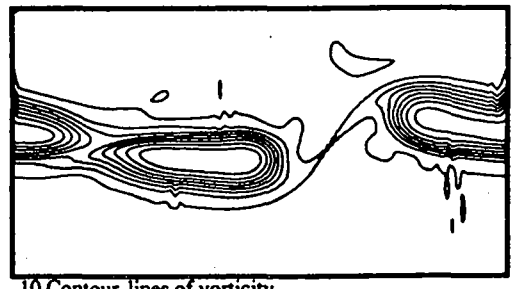

10 Contour-lines of vorticity
Distance between isovalues : 0.44636E-01
Min./ Max. real -0.36957 , 0.32157E-01
Min./ Max. used -0.36957 , 0.32157E-01
t = 330.01

Figure 28: Contour lines of two-structure-computation for two times, t=250 and t=330, 401 * 101 grid points, $Ma_c = 0.8$, $Re = 1000$, $Pr = 0.7$, $L_x = 45.04 \cdot \delta_i$, random perturbation

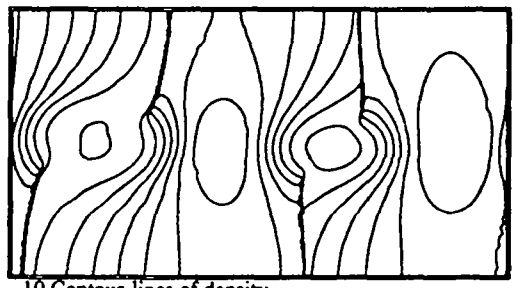

10 Contour-lines of density
Distance between isovalues : 0.10735
Min./ Max. real 0.39775 , 1.3639
Min./ Max. used 0.39775 , 1.3639
t = 250.14

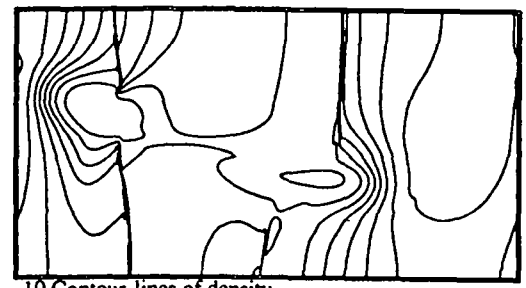

10 Contour-lines of density
Distance between isovalues : 0.87661E-01
Min./ Max. real 0.59433 , 1.3833
Min./ Max. used 0.59433 , 1.3833
t = 330.13

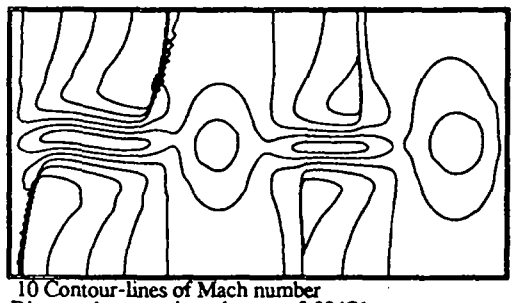

10 Contour-lines of Mach number
Distance between isovalues : 0.22471
Min./ Max. real 0.96443E-02 , 2.0320
Min./ Max. used 0.96443E-02 , 2.0320
t = 250.14

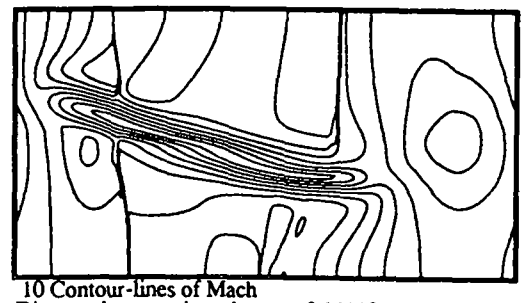

10 Contour-lines of Mach
Distance between isovalues : 0.14112
Min./ Max. real 0.56046E-02 , 1.2757
Min./ Max. used 0.56046E-02 , 1.2757
t = 330.13

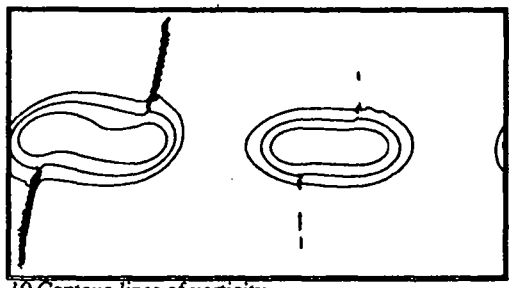

10 Contour-lines of vorticity
Distance between isovalues : 0.10352
Min./ Max. real -0.47563 , 0.45602
Min./ Max. used -0.47563 , 0.45602
t = 250.14

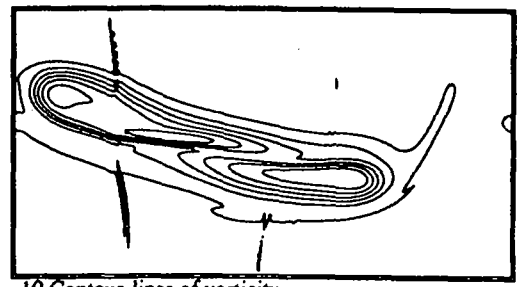

10 Contour-lines of vorticity
Distance between isovalues : 0.66822E-01
Min./ Max. real -0.41521 , 0.18619
Min./ Max. used -0.41521 , 0.18619
t = 330.13

Table 5: Comparaison of extreme values of contour lines, computation with shock

Extreme value	101 * 101 points	401 * 101 points	Difference (%)
rho_{min}	0.5945	0.5943	0.03
rho_{max}	1.3887	1.3833	0.39
Ma_{min}	$1.58 \cdot 10^{-2}$	$5.60 \cdot 10^{-3}$	—
Ma_{max}	1.3305	1.2757	4.29
ω_{min}	-0.3696	-0.4152	10.98
ω_{max}	0.0322	0.1862	—

Figure 29: Evolution of vorticity thickness for different number of points in x, random perturbation, $Ma = 0.8$, $Re = 1000$, $Pr = 0.7$, $L_x = 45.04 \cdot \delta$

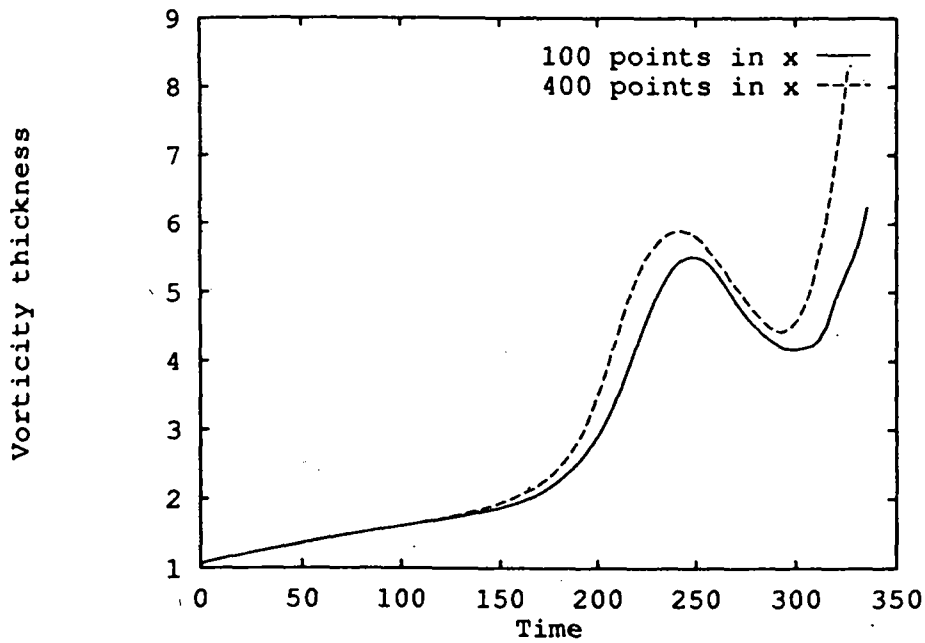

6.4 Simulation with four structures

In this section, we essentially comment upon the stabilizing effect due to the viscous growth of the shear layer with regard to the last simulation 6.3. To explain why we get two structures instead of four we consider Fig. 30 that shows the amplification factor $\alpha * c_i$ as function of the wavenumber $\alpha = \frac{2 \cdot \pi}{\lambda}$ according to linear, inviscid analysis of stability [11]. The basic velocity-profile is

$$u(y) = \tanh(2 \cdot y) \tag{52}$$

Fig. 29 suggests, that at the beginning of the last simulation 6.3 the dominant effect is the viscous growth of the shear layer and not the linear amplification of small disturbances. It seems, that the viscous growth nearly doubles its thickness. For a linear analysis of a two-times thicker basic-profile it turns out, that the shape of the stability-curves of fig. 30 does not change, but the curves are "compressed" in α-direction by a factor of 0.5. So the most amplified wavelength and the critical wavelength, where the stabilty-curve becomes negative, becomes two times longer too.

According to this explanation, if one starts with a perturbation whose wavelength has exactly the lenght of the most amplified mode λ_{max}, the viscous growth of the shear-layer is going to stabilize this disturbance and the first subharmonic (wavelength $\frac{\lambda_{max}}{2}$) is becomes more and more unstable as the shear layer thickness grows. This can explain, why in the preceeding simulation only two vortices appear instead of four.

One remedy against this stabilizing effect is to add a forcing term to the right-hand side of the Navier-Stokes equations. Here, instead we simply choose to use a larger box-length L_x, in this case approximately $2 \cdot L_x$. This led to the following simulation:

$$Ma = 1.6 \quad (i.e. Ma_c = 0.8), \qquad Re = 1000, \qquad Pr = 0.7 \tag{53}$$

$$L_x = 80 \cdot \delta_i \qquad L_y = 40 \cdot \delta_i \tag{54}$$

The grid was $201 * 101$-points-grid and the stretching-factor was $\alpha = \frac{1}{4}$. Fig. 34 shows the evolution of the vorticity thickness with time. Fig. 31, 32 and 33 show the contour-lines at the corresponding times $t = 200$, $t = 280$ and $t = 400$. At $t = 200$ four vortices can clearly be seen, while at $t = 280$, the

four vortices have paired into two big vortices. At the time $t = 400$ only one big vortex consisting of four smaller structures is left. This suggests that the preceeding explanation is basically correct.

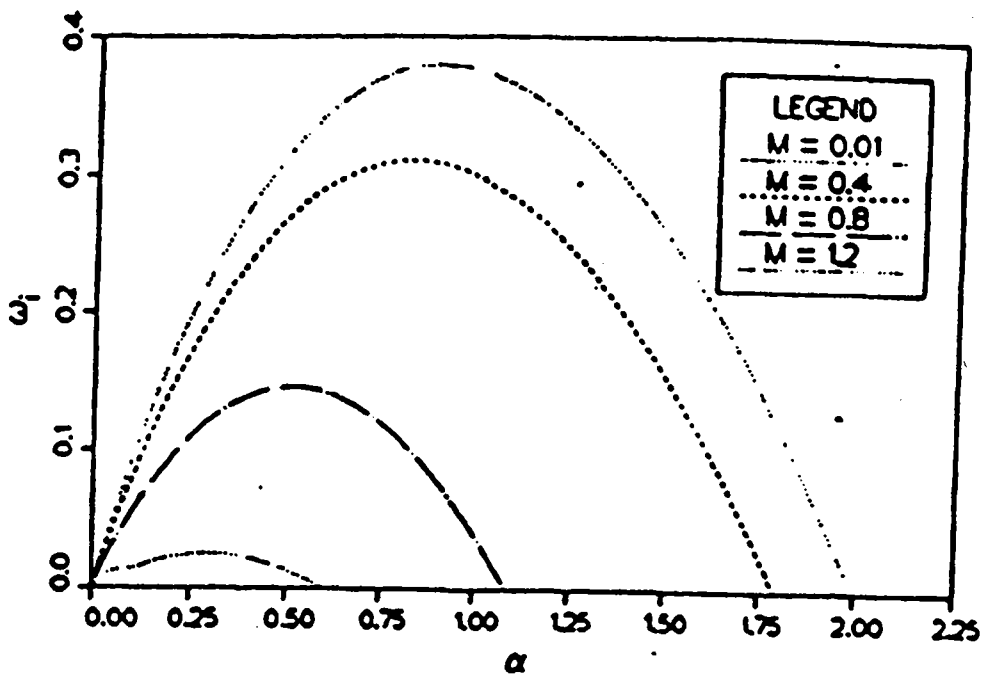

Figure 30: Stability curves for $u(y) = \tanh(2 \cdot y)$ according to linear, inviscid analysis of stability, from (14)

Figure 31: Contour lines of the four-vortex simulation $Ma_c = 0.8$, $Re = 1000$, $Pr = 0.7$, $L_x = 80 \cdot \delta_i$, $t = 200$

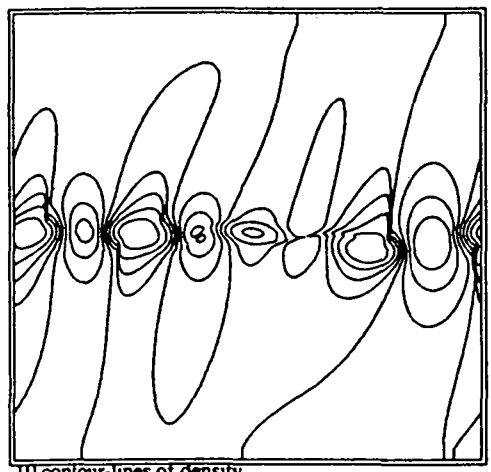

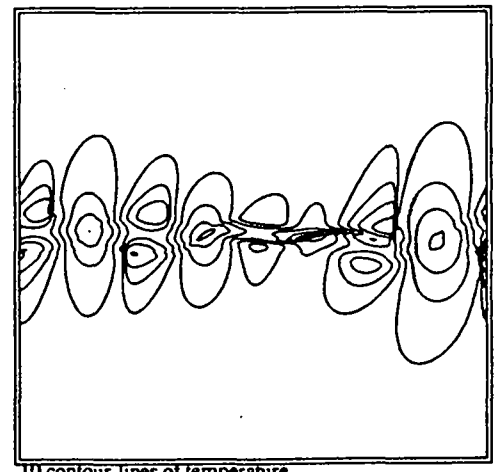

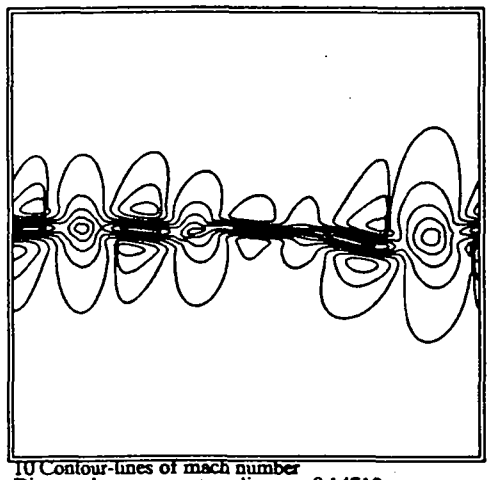

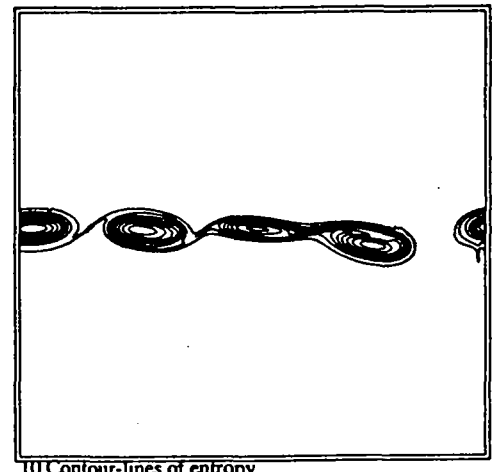

Figure 32: Contour lines of the four-vortex simulation, $Ma_c = 0.8$, $Re = 1000$, $Pr = 0.7$, $L_x = 80 \cdot \delta_i$, $t = 280$

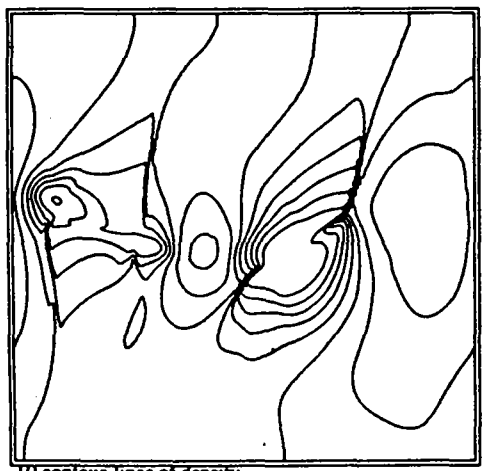

10 contour-lines of density
Distance between contour-lines : 0.10996
Min./ Max. real 0.35267 . 1.3423
Min./ Max. used 0.35267 . 1.3423
t = 280.15

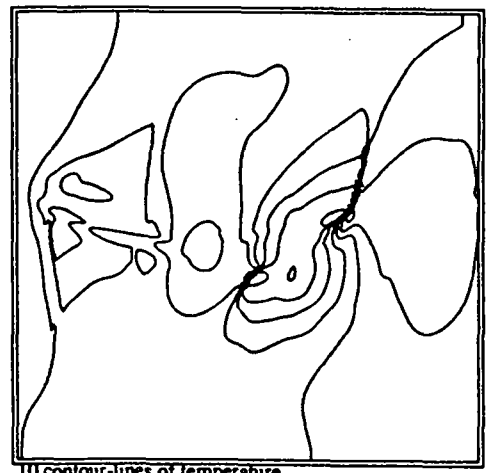

10 contour-lines of temperature
Distance between contour-lines: 0.65767E-01
Min./ Max. real 0.62082 . 1.2127
Min./ Max. used 0.62082 . 1.2127
t = 280.15

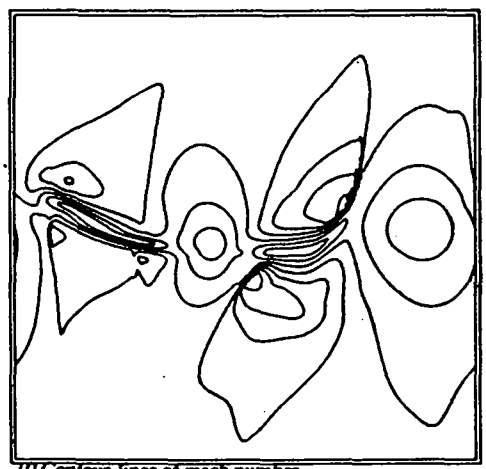

10 Contour-lines of mach number
Distance between contour-lines: 0.21978
Min./ Max. real 0.56976E-02 . 1.9837
Min./ Max. used 0.56976E-02 . 1.9837
t = 280.15

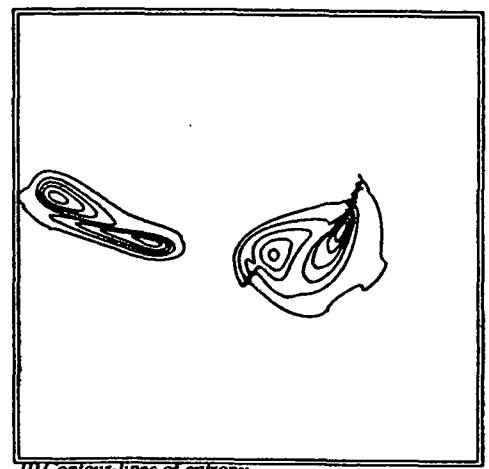

10 Contour-lines of entropy
Distance between contour-lines: 0.13952E-01
Min./ Max. real 0.24306 . 0.36863
Min./ Max. used 0.24306 . 0.36863
t = 280.15

Figure 33: Contour lines of the four-vortex simulation, $Ma_c = 0.8$, $Re = 1000$, $Pr = 0.7$, $L_x = 80 \cdot \delta_i$, $t = 400$

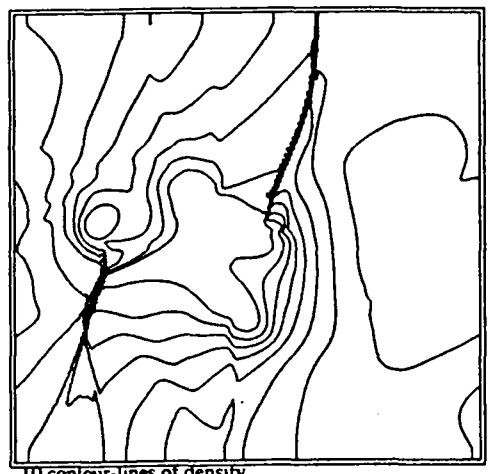

10 contour-lines of density
Distance between contour-lines: 0.11149
Min./ Max. real 0.36410 . 1.3675
Min./ Max. used 0.36410 . 1.3675
t = 400.18

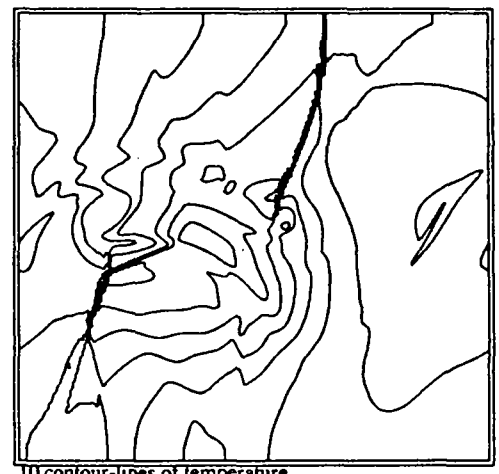

10 contour-lines of temperature
Distance between contour-lines: 0.57189E-01
Min./ Max. real 0.68636 . 1.2011
Min./ Max. used 0.68636 . 1.2011
t = 400.18

10 Contour-lines of mach number
Distance between contour-lines: 0.17575
Min./ Max. real 0.26133E-02 . 1.5844
Min./ Max. used 0.26133E-02 . 1.5844
t = 400.18

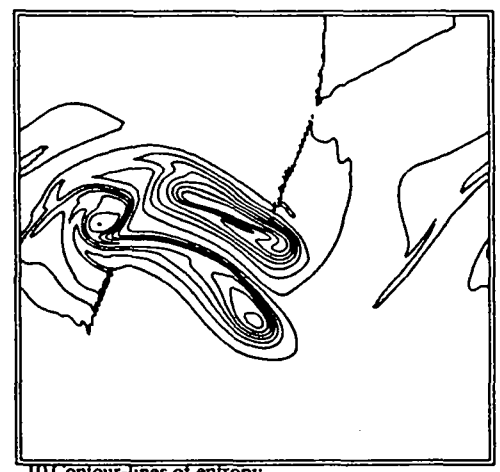

10 Contour-lines of entropy
Distance between contour-lines: 0.93386E-02
Min./ Max. real 0.26336 . 0.34740
Min./ Max. used 0.26336 . 0.34740
t = 400.18

Figure 34: Evolution of vorticity thickness for the four-structures simulation $Ma = 0.8$, $Re = 1000$, $Pr = 0.7$, $L_x = 80 \cdot \delta_i$

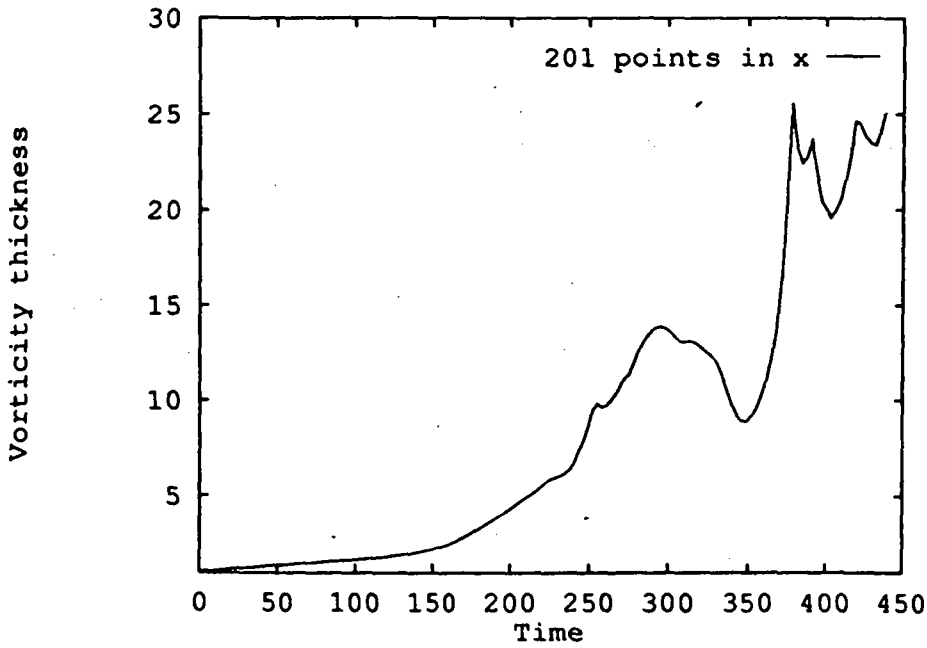

7 Conclusion

A large number of direct numerical simulations of compressible transitional flows are nowadays conducted with TVD-schemes. Although these methods are highly successful for steady computation, several recent studies reveal that both grid resolution and constituent limiters of the TVD schemes may influence the accuracy of the numerical simulation. This study attempts to validate the use of second order TVD schemes for the direct simulation of compressible mixing-layer : First, we have investigated shock-free configurations and compared the results obtained with a second order scheme with those obtained with a highly accurate spectral method. We concluded that accurate simulations can be reached with a moderate number of grid points.

However, when the convective Mach number is increased, (section 6) the simulations is much more sensitive to the resolution:
Even the simple one-structure computation at low Reynolds number displayed in section 6 shows that the detailed structure of the flow is not very well described in a 101 points simulation. Moreover, the examination of the spectra of the "compressible" and "incompressible" parts of the flow reveals that this lack of resolution is not entirely related to the emergence of shocks, but that the "incompressible" part (expected to be more regular) is also not well resolved.

The situation becomes worse when two structures computations are performed: As already noted by Atkins [1], there is a spurious amplification of the subharmonic mode that influences strongly the time when pairing occurs. Consequently if the most exited mode is not the longest wave supported by the domain, an unphysical energy transfer to the subharmonics will occur and eventually dominate the numerical results. The situation is a little bit better when the different modes are exited at roughly the same amplitude as in the computations done with random perturbations. However, even in this case low resolution computations show some delays with respect to high resolution runs.

Thus the simulation of compressible mixing layers is much more difficult than comparable studies in the incompressible regime. No adequate numerical method seems to exist nowdays : The simulation of transitional flows with

second-order TVD like schemes must be restricted to low convective Mach number flows. For larger convective Mach-numbers, further studies must be conducted to identify reliable numerical methods. As an example of the type of methods that have some potential in this direction, in a forthcoming study we will report on similar experiments using high-order ENO schemes.

References

[1] H. L. Atkins, Analysis of a second-order-accurate finite-volume method for temporally growing compressible shear layers, AIAA Paper No. 89-1809.

[2] W. Blumen, Shear layer instability of an inviscid compressible fluid, J. Fluid Mech. vol. 40, part 4 (1970), pp 769 - 781.

[3] W. Blumen, P. G. Drazin and D. F. Billings, Shear layer instability of an inviscid compressible fluid, Part. II, J. Fluid Mech. vol. 71 (1975), pp 305 - 316.

[4] H. Guillard, J. M. Malé and R. Peyret, Adaptive Spectral Methods with Application to Mixing Layer Computations, J. Comp. Phys., vol. 102, (1992), pp 114 - 127.

[5] A. Michalke, On the inviscid instability of the hyperbolic-tangent velocity profile, J. Fluid Mech., 1964

[6] S. K. Lele, Direct Numerical Simulation of Compressible Free Shear Flow, AIAA Paper 89-0374, 1989

[7] P. J. Lu and K. C. Wu, Assessment of Total Variation Diminishing Schemes in Compressible Mixing Flow Computations, AIAA Journal, Vol. 30, p. 939-946, 1992.

[8] M. Meinke and D. Hänel, Simulation of unsteady flows, 12th Int. Conf. on Num. Meth. in Fluid Dynamics, Oxford 1990, Lecture Notes in Physics 371.

[9] P. L. Roe, Approximate Riemann Solvers, Parameter Vectors and Difference Schemes, Journal Computational Physics, 43, (1981), p. 357-372.

[10] C.-W. Shu, G. Erlebacher et al., High-Order ENO Schemes applied to two- and three-dimensional compressible flow, ICASE Report No. 91-38.

[11] N. Sandham and W. Reynolds, The Compressible Mixing Layer: Linear Theory and Direct Simulation, AIAA-Paper 89-0371.

[12] A. Tsilanizara, Simulation numérique de la couche de mélange compressible par méthode spectrale, thèse Université de Poitiers, 1988.

[13] B. van Leer, Towards the Ultimate Conservative Difference Scheme II. Monotonicity and Conservation Combined in a Second Order Scheme, J. Comp. Physics, vol. 14, p. 361 - 370, (1974).

[14] N. D. Sandham, and H. C. Yee, A Numerical Study of a Class of TVD Schemes for Compressible Mixing Layers, NASA Technical Memorandum No. 10 21 94, 1992.

Unité de Recherche INRIA Sophia Antipolis
2004, route des Lucioles - B.P. 93 - 06902 SOPHIA ANTIPOLIS Cedex (France)

Unité de Recherche INRIA Lorraine Technopôle de Nancy-Brabois - Campus Scientifique
615, rue du Jardin Botanique - B.P. 101 - 54602 VILLERS LES NANCY Cedex (France)
Unité de Recherche INRIA Rennes IRISA, Campus Universitaire de Beaulieu 35042 RENNES Cedex (France)
Unité de Recherche INRIA Rhône-Alpes 46, avenue Félix Viallet - 38031 GRENOBLE Cedex (France)
Unité de Recherche INRIA Rocquencourt Domaine de Voluceau - Rocquencourt - B.P. 105 - 78153 LE CHESNAY Cedex (France)

EDITEUR
INRIA - Domaine de Voluceau - Rocquencourt - B.P. 105 - 78153 LE CHESNAY Cedex (France)

ISSN 0249 - 6399